KING'S College LONDON

University of London

# 6CCYB070 BEng Research Project


# Development of a Physical C-Arm Simulator to Mimic Fluoroscopic Imaging of Transparent Phantoms Without Radiation Exposure

**Prithvish Ganguly**

**Supervisor: Professor Kawal Rhode**

Project Report submitted in partial fulfilment of
the Bachelor of Engineering degree in
**Biomedical Engineering**
**May 2025**

# Project Plan

## Problem

A C-Arm is a medical imaging device that produces real-time images using X-ray radiation. Although exposure to X-ray radiation is deemed generally safe for patients undergoing procedures, it poses a serious problem for healthcare professionals who work with these imaging devices as they are constantly exposed to X-ray radiation for long periods of time. Currently, the primary solution for this is lead-protective garments which minimise the exposure to ionising radiation, however, due to the very high density of lead, these garments are heavy and can be very uncomfortable if worn for extended periods. This can lead to an increased risk of musculoskeletal disorders in healthcare professionals and researchers which negatively affects their quality of life, work output, and general wellbeing. Another problem for current C-arm X-ray imaging systems is their cost, size, and complexity which makes them impractical to use to train medical professionals in surgical procedures that require this imaging system and in certain fields of scientific research e.g. phantom development.

## State of the Art

Currently, C-arm X-ray simulators rely on expensive systems such as digitally reconstructed radiographs (DRRs), fluoroscopy-based methods, or virtual reality setups. Although they help mitigate radiation exposure for healthcare professionals and researchers, these systems are often expensive, non-portable, and reliant on complex hardware which limits their accessibility. The proposed system introduces a novel approach combining cost-effective webcam-based imaging with artificial intelligence to generate real-time, X-ray-like images. This method does not require the use of ionising radiation or expensive imaging equipment. Additionally, the system's modularity and portability address the shortcomings of traditional simulators, making it accessible and a practical choice for a broader range of users.

## Aims

The primary aim of this project is to create a portable and cost-effective C-arm X-ray simulator that addresses the challenges of traditional systems while making training more accessible and realistic. It aims to deliver X-ray-like images of transparent organ phantoms using webcam-based imaging utilising AI-driven image processing. This eliminates the need to use ionising radiation, providing a safe and effective alternative to conventional imaging for phantoms used in research and medical training. The system will also feature preset positions to mimic commonly used C-arm configurations, making it practical for procedural training. Lastly, the system will aim to have a modular and portable design which will allow it can be easily adapted to a wide range of training and research environments.

## Work Plan

I began working on this as my KURF project in June 2024, where I built upon previous research work on this simulator and improved the design, efficiency and robustness of the simulator. This project will continue development of the simulator from that stage and the system will be developed in three phases.

**Phase 1:**

The first phase will focus on designing and assembling the hardware, including finalising the C-arm mounting system, creating a 3D-printed phantom base, and installing multiple light sources with polarised filters to improve image clarity. In this phase, numerous hardware components will be improved making the simulator more robust and reliable.

**Phase 2:**

The second phase will focus on developing computer programs to control stepper motors and program preset C-arm positions to replicate standard configurations. Additionally, during this phase, I will also train and integrate an AI model, such as CycleGAN, to process webcam data into X-ray-like visuals.

**Phase 3:**

The third phase will focus on testing and refining the system by evaluating its functionality and performance under realistic conditions. Any issues identified will be addressed to ensure the simulator is reliable and effective.

**Report writing and Documentation:**

Finally, I will write the dissertation report, detailing the design, implementation, and outcomes of the simulator, and prepare a presentation to showcase the project's findings.

## Deliverables

The project will result in the development of a functional C-arm simulator that provides real-time, AI-driven X-ray-like imaging. It will include preset positions for replicating standard configurations, portable and modular hardware with a 3D-printed phantom base, and polarised lighting for enhanced image quality. Comprehensive documentation will be produced, detailing the design, implementation, and evaluation processes. The deliverables will also include a final presentation demonstrating the simulator's capabilities for training and procedural simulation.

## Evaluation

The success of this project will be determined by evaluations provided by Professor Kawal Rhode and an NHS-certified radiologist. This will be done using a questionnaire that will score each aspect of the user experience, such as ease of use, functionality, robustness and similarity to traditional fluoroscopic images. This will help determine the usability of the simulator in medical training and research.

## Project Timeline

| | OCT-15 | NOV-15 | DEC-15 | JAN-14 | FEB-14 | MAR-1 | APR-01 |
|---|---|---|---|---|---|---|---|
| **Phase 1** | | | | | | | |
| **Phase 2** | | | | | | | |
| **Phase 3** | | | | | | | |
| **Report** | | | | | | | |

**Fig1.** Project Timeline.

# Acknowledgements

I would like to thank Professor Kawal Rhode for his continued guidance throughout this project, particularly in helping shape its core direction and for providing key insights during design and testing phases. His advice was instrumental in the decision to transition to a single-unit C-arm, and he also played a critical role during the experimentation process, operating the clinical fluoroscopy C-arm and conducting the real-time imaging procedures. I am especially grateful for his support in helping fabricate the C-arm using the Chiron 3D printer and in troubleshooting challenges that arose throughout the project.

I would also like to express my sincere thanks to Carlo Saija, whose involvement and support extended through all phases of development. He provided valuable assistance in Fusion 360 design, 3D printing, laser cutting, base assembly, and testing, as well as by participating in the user evaluation questionnaire.

I would like to thank members of Professor Rhode's research group for their thoughtful suggestions and encouragement throughout the process. In particular, I am thankful to Steven Morris and Zixi Wang for their feedback during development, and to Wei Zhao for his assistance with motor control integration. I would like to acknowledge the support of lab technician Jay Barrington, whose help with manufacturing specific parts and providing electrical training was invaluable to the completion of this project. I also would like to express my gratitude to Shuchishmita Maitra, Pablo Aparicio Villar, and Shawin Ananth for their contribution in the testing phase and data collection. Finally I would like to thank my family for their unwavering support through this entire journey.

# Abstract

This project developed a cost-effective, radiation-free C-arm simulator capable of generating fluoroscopy-like images of transparent phantoms using visible light and real-time image processing. A modular simulator was constructed using 3D-printed and laser-cut components, a wireless webcam, and a motorised control system. The imaging pipeline applied grayscale conversion, inversion, and edge detection to produce fluoroscopy-style output without the use of ionising radiation. Simulator performance was evaluated under backlight and dynamic floodlight lighting conditions across multiple anatomical angles, and images were cross-verified against real fluoroscopic references to qualitatively assess realism. User feedback was collected from experienced biomedical engineers, confirming mechanical stability, system responsiveness, and satisfactory imaging output at standard views. Limitations identified included lighting inconsistency at oblique angles, ROI misalignment, and a restricted sample size for user evaluation. Overall, the simulator demonstrated the feasibility of low-cost, sustainable fluoroscopy simulation, providing a foundation for future improvements in medical training, device testing, and imaging system development.

# Table of Contents

# List of Figures

# List of Tables



# List of Equations



# List of Abbreviations

**AP** – Anterior–Posterior

**RAO** – Right Anterior Oblique

**LAO** – Left Anterior Oblique

**ROI** – Region of Interest

**CAD** – Computer-Aided Design

**FDM** – Fused Deposition Modelling

**PLA** – Polylactic Acid (3D Printing Filament)

**DC** – Direct Current

**IDE** – Integrated Development Environment

**EEPROM** – Electrically Erasable Programmable Read-Only Memor

# 1. Introduction and Background

## 1.1 Clinical Motivation and Radiographic Principles

X-rays are a form of high-energy electromagnetic radiation and are a fundamental modality in medical imaging. They belong to the electromagnetic spectrum, encompassing a range of radiant energy propagated through space as waves and photons, similar to visible light and radio waves [1]. X-rays are characterised by their short wavelengths, typically between 0.01 nm and 10 nm (**Figure 1 Part A**), and possess high energy levels, ranging from 100 eV to 120 keV [1]. This elevated energy gives X-rays the ability to penetrate various materials, including biological tissues, a property central to their application in medical imaging [1]. The discovery of X-rays in 1895 by Wilhelm Conrad Röntgen marked a pivotal moment (**Figure 1 Part B**), leading to their rapid integration into diagnostic practices worldwide [1]. Today, X-ray imaging is routinely used in a multitude of clinical scenarios, ranging from the detection of skeletal fractures to guiding minimally invasive interventions [1].

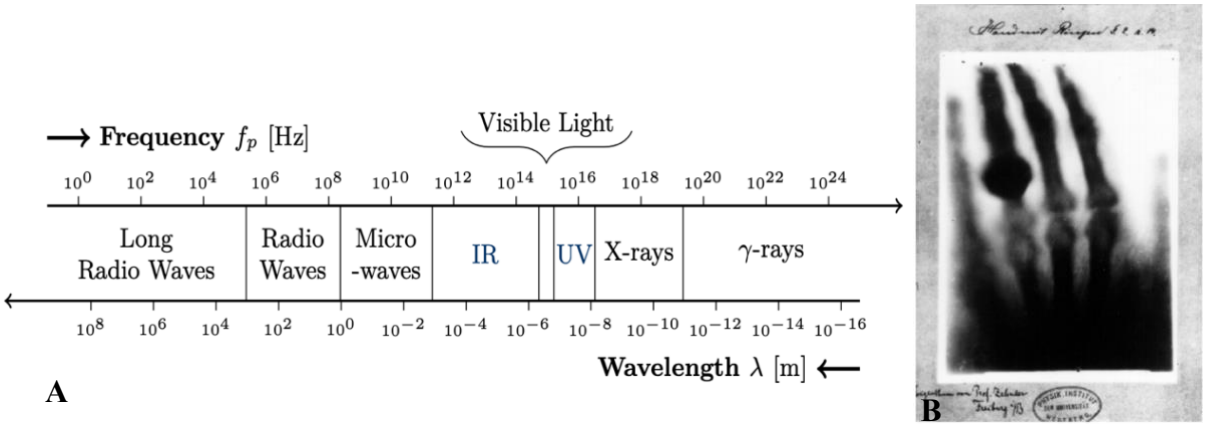


***Figure 1. A:*** *Frequencies and wavelengths of the different forms of electromagnetic radiation. X-rays have a wavelength in the range of 0.01 nm up to 10 nm [1].* ***B:*** *One of the first X-rays taken in history: an image of Wilhelm Röntgen's wife's hand [1].*

In medical imaging, X-rays are used to visualise the internal structures of the body based on the principle of differential attenuation [1, 2]. As X-ray photons travel through tissues, they undergo absorption and scattering, the extent of these interactions are determined by the tissue's density and atomic composition [1, 2]. Denser materials, such as bone and calcifications, attenuate a greater proportion of X-ray photons compared to less dense tissues like air, fat, and soft tissue [2]. This differential attenuation results in a spatial variation in the intensity of the X-ray beam that emerges from the patient (**Figure 2 Part A**) [1]. This exiting beam then interacts with a detector, such as a film or a digital detector, to create an image representing the internal anatomy [2]. Typically, radiography is capable of resolving four primary density levels: air, fat, soft tissue, and calcification, providing valuable diagnostic information [2]. Furthermore, in situations where the natural contrast between tissues is insufficient, exogenous contrast agents can be administered [2]. These agents, such as barium and iodine (positive contrast) or air and carbon dioxide (negative contrast), alter the local X-ray attenuation, enhancing the visualisation of specific structures like blood vessels or the gastrointestinal tract (**Figure 2 Part B)** [2].

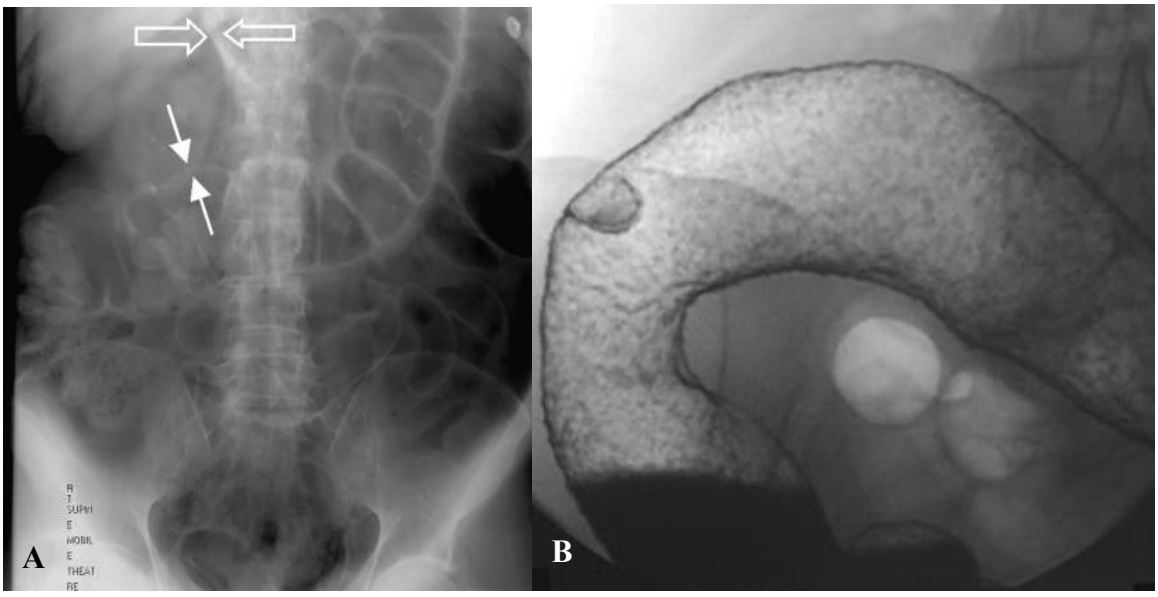


***Figure 2. A:*** *X-ray showing how gas (white arrows) outlines internal structures. The open arrows highlight a central structure made visible by surrounding gas, demonstrating differences in X-ray absorption [2].* ***B:*** *X-ray of colon using barium as a contrast agent, allowing clearer visualisation of a 3-cm polypoid carcinoma [2].*

## X-ray Generation

The formation of an X-ray image relies on the interaction of X-ray photons with the patient's tissues and subsequent detection [1,2]. When an X-ray beam passes through the body, the number of photons reaching the detector is reduced based on the attenuation properties of the intervening tissues [1]. This reduction in intensity follows an exponential relationship described by Lambert-Beer's law (**Equation 1**), where the intensity of the transmitted X-rays, $I(x)$ , is inversely proportional to the thickness($x$) and attenuation coefficient of the material($\mu$) [2].

$$I(x) = I_o \times e^{-\mu x}$$

***Equation 1**: Lambert-Beer Law*

$$I(x) \propto e^{(-\mu x)}$$

***Equation 2**: Exponential attenuation of X-ray intensity as a function of material thickness and attenuation coefficient, illustrating the inverse relationship described by Lambert-Beer's law.*

The attenuation of X-rays is primarily due to three key interaction mechanisms within the diagnostic energy range: 1) photoelectric effect, 2) Compton scattering, and 3) Rayleigh scattering (**Figure 3**) [1] . The photoelectric effect involves the complete absorption of an X-ray photon by an inner-shell electron of an atom, leading to the ejection of a photoelectron [1]. Compton scattering involves the interaction of an X-ray photon with an electron, resulting in the scattering of a lower-energy photon at an angle and the ejection of a recoil electron [1]. Rayleigh scattering is a coherent process where a low-energy photon interacts with electrons, causing them to vibrate and emit a photon of the same wavelength but potentially different direction, without energy loss or ionization [1]. The varying degrees to which these interactions occur in different tissues are fundamental to the contrast observed in an X-ray image [1]. The spatial distribution of the attenuated X-ray beam is then captured by a detector, which converts the X-ray energy into a visible image or a digital signal that can be processed and displayed

[1,2]. Modern X-ray detection systems include image intensifiers and flat panel detectors, which offer real-time imaging and digital capabilities, respectively [1].

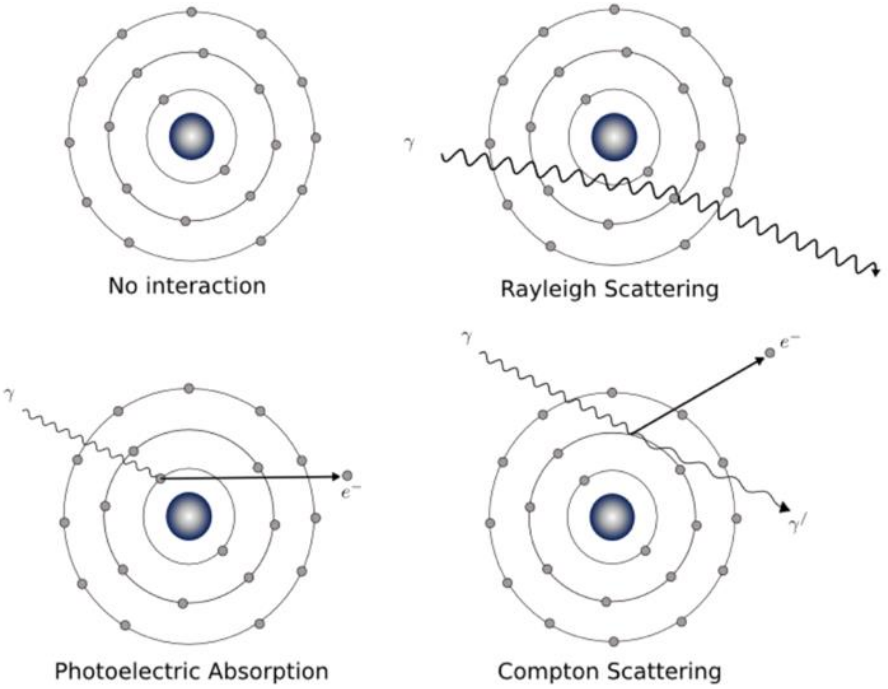


***Figure 3.*** *Key interactions between X-ray photons and matter: no interaction, Rayleigh scattering, photoelectric absorption, and Compton scattering. These processes determine how X-rays are attenuated in tissues, forming the basis of image contrast.[1]*

## Effects of Ionising X-Ray Radiation on Healthcare Professionals

Ionising radiation is a high-energy radiation capable of damaging biological tissue at an atomic and molecular level [3]. In the medical field, this type of radiation is utilised in various diagnostic and interventional procedures, leading to potential occupational exposure for healthcare professionals involved [3, 4, 5]. The primary concern associated with exposure to ionising radiation is the increased risk of stochastic effects, such as cancer, which are probabilistic and may occur long after exposure [3-8]. Deterministic effects, which have a threshold dose and increase in severity with dose, such as cataracts, can also be a concern with higher levels of exposure [4-8]. The concept of effective dose is used to quantify the risk from exposure to different types and energies of radiation affecting various organs and tissues with differing sensitivities [3,9]. A study found that a physician regularly performing fluoroscopically guided interventional procedures with appropriate protection could expect an

annual occupational radiation dose of 2–4 mSv [10]. It is also noted that considerable variability in typical radiation doses to physician operators has been observed in the past [10]. While definitive 'safe' levels of low-level chronic radiation exposure are not explicitly established in these sources [8], the principle of keeping radiation exposure as low as reasonably achievable (ALARA) without compromising essential diagnostic information is a guiding principle [10]. Some studies examining occupational exposure have not consistently shown an increased risk of stochastic effects, but positive findings suggest a potential small risk that might be under detected [8]. Furthermore, there is evidence linking occupational radiation exposure to specific health issues in healthcare professionals. For instance, concerns have been raised regarding brain cancer incidence in interventional cardiologists and interventional radiologists [8], although the evidence for a causal link from low-level radiation exposure remains debated and potentially confounded by non-radiation factors or chance[8,10]. Radiation-induced cataracts are another documented concern, particularly for interventional cardiologists and radiologists (**Figure 4**) [6, 8] . One study noted a weak trend of increasing cataract prevalence with occupational dose in radiologic technologists, with a stronger trend associated with personal diagnostic radiographs [10].

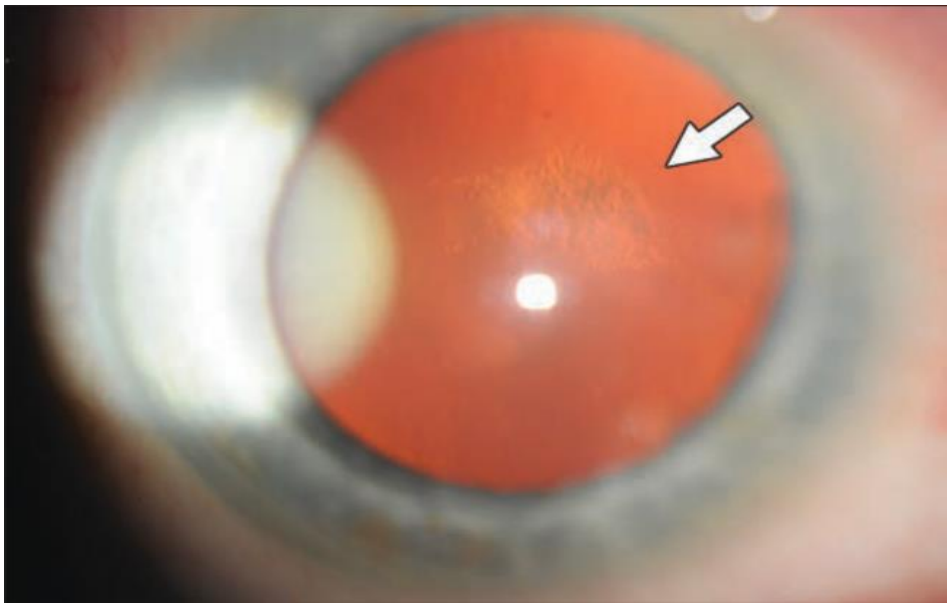

***Figure 4.*** *Image of patient with posterior subscapular cataract, predominant type of radiation induced cataract [8]*

## Use of Lead Shielding for Radiation Protection

The cornerstone of radiation protection for healthcare professionals in fluoroscopic environments has been the use of physical shielding, primarily in the form of lead aprons (**Figure 5 Part A**) and fixed or portable barriers [5,11]. These protective garments and devices work by attenuating the incident X-ray radiation, thereby reducing the dose received by the wearer [4,5,12]. Lead, due to its high atomic number and density, is an effective material for absorbing X-rays within the energy ranges typically used in medical imaging[12]. Lead aprons are commonly manufactured from lead impregnated with materials such as polyvinyl chloride (PVC), rubber, or emulsion polymers[12]. They are available in various lead equivalent thicknesses, typically ranging from 0.25 mm to 0.5 mm, with the choice depending on the anticipated radiation exposure levels and the type of protective garment used (Figure 5 part B). [4,12,13].

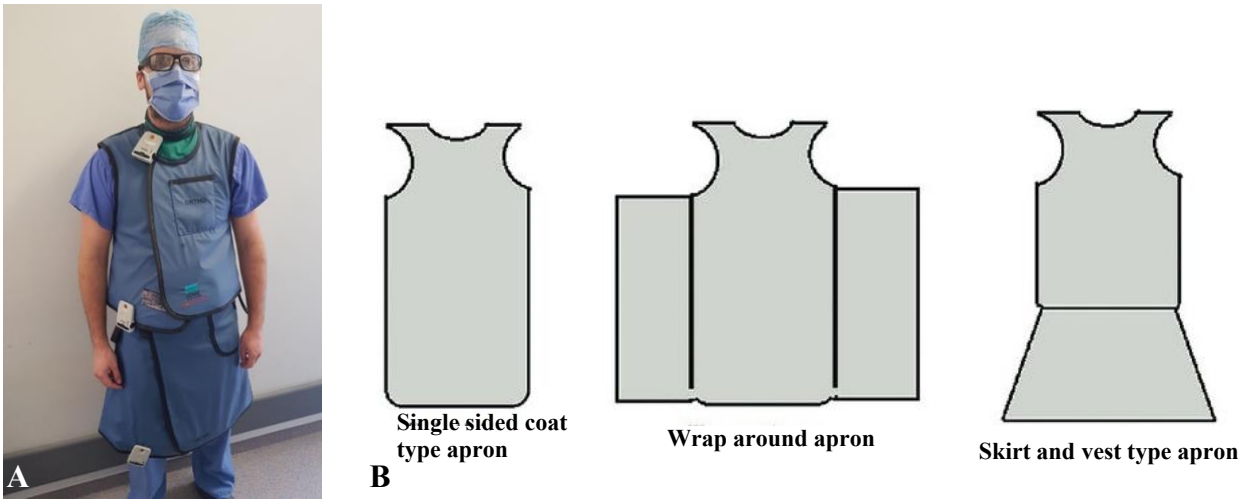


***Figure 5. A:*** *Radiologist wearing a skirt and vest type lead apron [14].* ***B:*** *Examples of different models of commonly used radiation protective aprons [13].*

While lead aprons are effective at reducing radiation exposure, with the potential to reduce it by up to 99% depending on thickness and correct use [11], they present several significant drawbacks, particularly concerning their physical and ergonomic impact on daily users [4,12]. The weight of these aprons is a major concern as most lead aprons weigh approximately 7 kg

[4], and a 15-pound (6.8kg) apron has been estimated to exert pressures of up to 300 pounds per square inch (2 kPa) on the intervertebral discs[11,15]. This additional axial loading and the constant burden of carrying this weight during often lengthy procedures have been increasingly associated with a higher prevalence of musculoskeletal disorders (MSDs) among healthcare workers who regularly wear them [3,12,15]. Studies have indicated a significant potential for injury associated with wearing lead aprons in healthcare settings, with a meta-analysis of cross-sectional studies revealing a combined odds ratio of 3.83 for musculoskeletal disorder prevalence in lead apron wearers compared to a baseline population [4]. One particular study reported that 47% of interventionalists in the study had body aches due to wearing single-sided aprons and interventionists working more than 10 hours per day wearing single-sided lead apron mainly complained of back pain and shoulder pain [13]. This increased prevalence can lead to reduced work capacity and even career-ending injuries [4]. Specific issues reported include back pain, neck pain, and shoulder pain [12,15], with some research identifying 'interventionalist's disc disease' as a potential consequence of prolonged lead apron use [11]. While one study did not find a correlation between the prevalence of back pain and the duration of lead apron use [11], however another study found that employees with lead apron use experienced work-related musculoskeletal pain more often than a control group [4]. Furthermore, wearing lead aprons can lead to altered body kinematics [4], potentially contributing to musculoskeletal strain. The weight distribution and forces exerted on the body by these aprons can cause significant pressure in intervertebral disc spaces [4].According to a survey of 630 staff members within a radiology department, technologists accounted for the largest proportion of reported work-related injuries at 67% (**Figure 6 Part A**)[16]. Furthermore, the survey also found that the majority of these injuries were attributed to repetitive stress arising from improper ergonomics (**Figure 6 Part B**), which can be exacerbated by factors such as prolonged use of lead aprons[16].

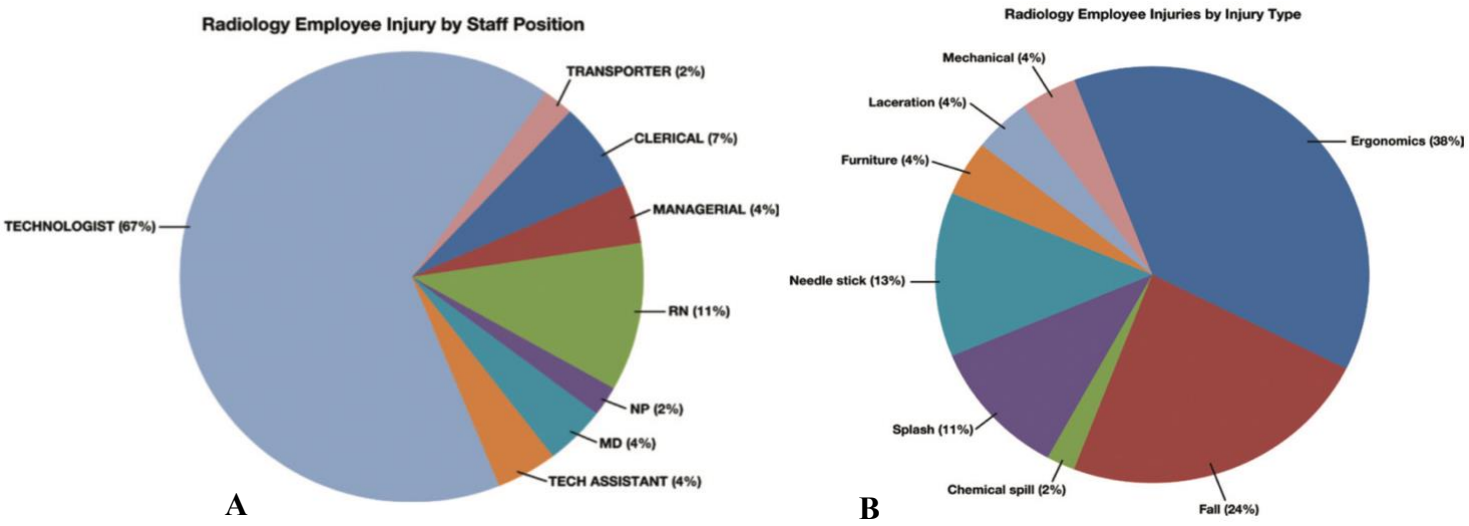


***Figure 6. A****: Injuries among radiology department staff were most commonly reported in technologists, likely due to the physically demanding nature of their work and frequent patient interaction. Abbreviations: MD – medical doctor; NP – nurse practitioner; RN – registered nurse; Tech – technologist [16].* ***B****: Injuries among radiology department employees by type showed that the majority resulted from repetitive strain, often caused by poor ergonomic practices [16].*

Beyond the weight, other drawbacks of traditional lead aprons exist. They can be uncomfortable due to heat insulation and thermal discomfort, especially with multi-layered designs [12]. Hygiene is also a concern, as aprons can pick up dirt and become contaminated with germs, potentially causing infections [12]. The often generic design and sizing charts may not adequately fit diverse body shapes, affecting both comfort and potentially the effectiveness of protection [12]. Defects such as holes, tears, and cracks, which can occur with use and improper storage, can compromise the shielding ability of the aprons (**Figure 7 Parts A & B**) [12]. Despite these issues, regulatory requirements for wearing heavy lead aprons have changed little since the late 1920s [4].In light of these limitations, there is a growing need to consider alternative radiation protection methods and ergonomic interventions to mitigate the physical burden associated with lead aprons while maintaining adequate radiation safety for healthcare professionals [4,6].

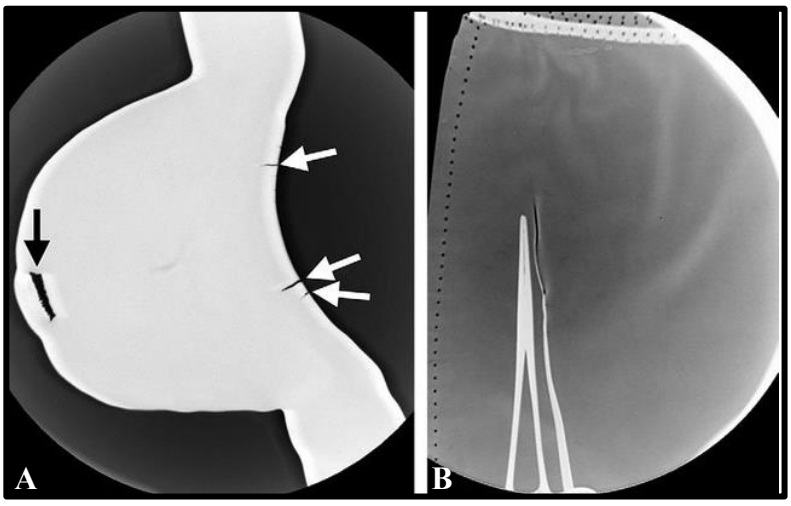


***Figure 7*** *Radiographs demonstrating damaged protective gear.* ***A:*** *Multiple small cracks are visible along the upper edge of the thyroid shield (white arrows), with a larger defect seen lower down (black arrow).* ***B:*** *A long crack is evident in the skirt portion of a lead apron, with a Kelly forceps placed adjacent to the crack for size reference* ***[16]***

## 1.2 Fluoroscopy and C-arm Systems in Medical Imaging

Fluoroscopy is a medical imaging technique based on X-rays that enables the visualisation of real-time processes within the human body [17]. This dynamic imaging capability is crucial when observing movement or the progression of contrast agents, finding applications in a wide range of medical fields such as radiology, gastroenterology, surgery, pain management, and cardiology [17]. The fundamental principle of fluoroscopy involves the use of an X-ray tube as the source of radiation [17]. This device allows for independent control over the energy (kV) and number (mA) of X-rays produced [17]. X-rays are generated by accelerating electrons from a hot filament (cathode) towards a tungsten anode within an evacuated tube (**Figure 8**). The resulting interactions produce a spectrum of X-ray photons [17]. Initially, physicians directly viewed a fluorescent screen, however, contemporary systems predominantly utilise digital image receptors, marking a revolutionary shift from earlier analogue devices [17].

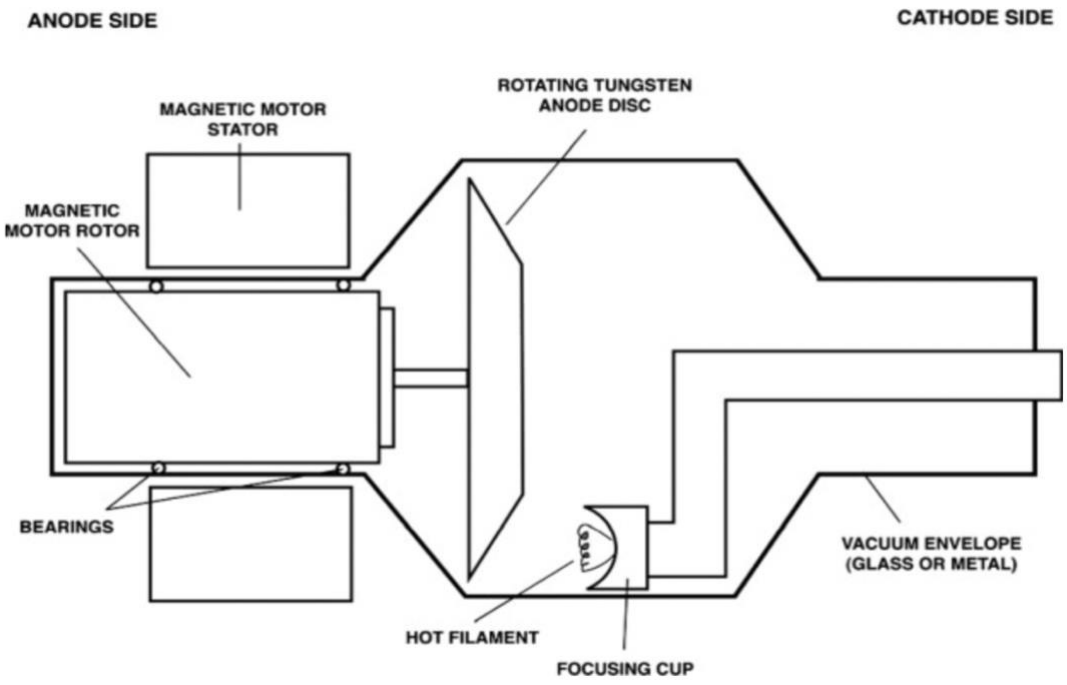


***Figure 8*** *Labelled X-ray tube schematic showing all the components used to produce X-rays for fluoroscopic imaging* ***[17]***

The necessity for real-time X-ray imaging during surgical procedures led to the development of C-arm systems. These systems are designed to perform both real-time motion or cine imaging series and the acquisition of still images[18]. These systems are designed to perform both real-time motion or cine imaging series and the acquisition of still images [18]. C-arm systems consist of an imaging receptor head, most commonly a flat panel detector and an X-ray tube mounted on opposite ends of a C-shaped support (**Figure 9**) [18]. Larger, fixed units are typically found in dedicated imaging suites, whereas smaller, mobile units can be easily moved to the location where the procedure is taking place [18]. A standard mobile C-arm system also includes monitors for image display, controls for setting exposure parameters and managing images, and warning systems that indicate radiation emission [18].

Mobile C-arm systems are engineered to be highly versatile, allowing for various movements to achieve optimal imaging during surgery, where patient positioning is primarily dictated by surgical access (**Figure 9 Part A**) [18]. Common C-arm movements include vertical movement of the C-arm, horizontal movement of the C-arm, right/left angulation, craniocaudal angulation (**Figure 9 Part B**) [18]. The base unit of a mobile C-arm is typically mounted on wheels that allow for free movement and steering, often with the capability to fix the unit's movement along a desired path. Modern mobile C-arm systems typically feature a multi-phase generator, which may be located in the base unit or the C-arm unit itself, providing consistent power to the X-ray tube. These generators often support high-frequency pulsed exposure settings for procedures like vascular angiography and lower current continuous output for general fluoroscopy [18]. The X-ray tube in a C-arm system is designed to be as light and small as possible to maintain mobility. Systems used for vascular imaging may include rotating anodes to manage the increased heat generated during high-output angiography runs, and may also have separate focal spots for different dose levels [18]. Lead collimators are integrated

within the beam path to shape and control the X-ray beam, allowing the operator to reduce scatter radiation, improve image detail, and minimise the irradiation of sensitive structures [18].

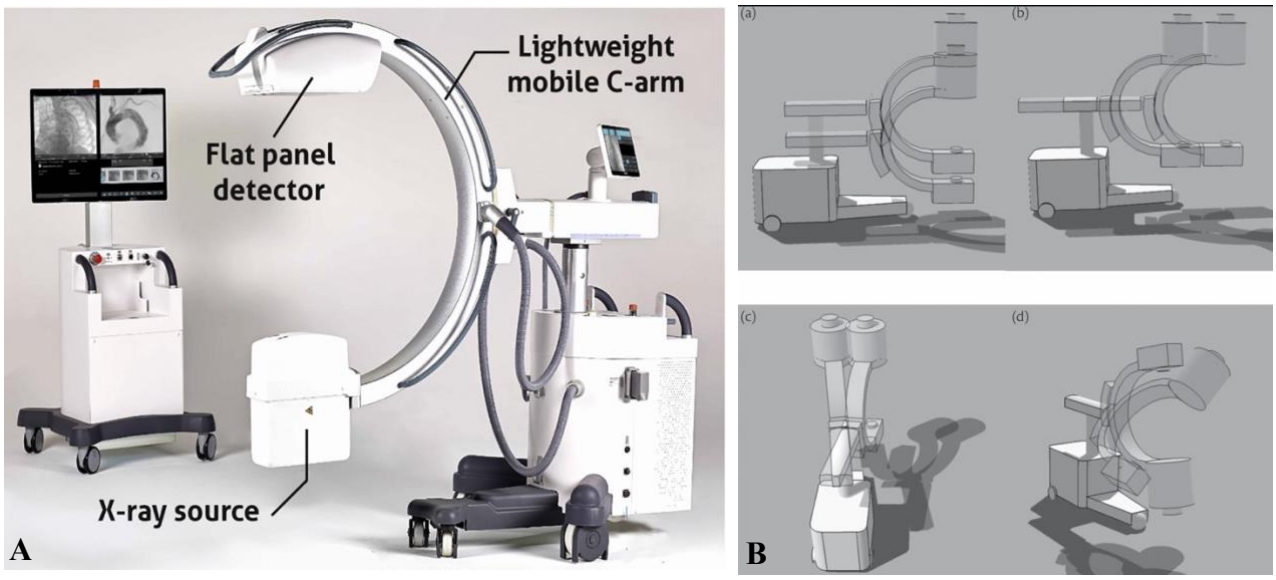


***Figure 9. A:*** *Labelled image of a commonly used mobile C-Arm system (ARCO FP by ATS) [19].* ***B:*** *Common C-arm movements.* ***(a)*** *Vertical movement of the C-arm.* ***(b)*** *Horizontal movement of the C-arm.* ***(c)*** *Right/Left angulation.* ***(d)*** *Craniocaudal angulation [18].*

## Robotic Fluoroscopic Procedures

Fluoroscopy serves as an essential diagnostic modality across numerous medical specialties due to its capacity for real-time evaluation [20]. Common fluoroscopic procedures include swallowing studies, upper and lower gastrointestinal (GI) imaging, angiography, and the placement of various medical devices such as stents, needles, lines, and tubes [17]. The field of medical robotics has seen the development of various systems for image-guided interventions, including procedures performed under fluoroscopic guidance [21]. These robotic systems are being explored for their potential to enhance the accuracy and safety of interventions. For instance, the AcuBot robot, developed at Johns Hopkins and Georgetown University, is designed to work with CT or fluoroscopy for active needle insertion in procedures such as nerve and facet blocks (**Figure 10 Parts A & B**) [21]. Clinical trials have been conducted using the AcuBot under fluoroscopy to precisely position needles for nerve blocks in the lumbar spine [21]. In these trials, fluoroscopy was used in the anteroposterior (A/P) view to position and orient the needle, and in the lateral view to monitor the depth of

insertion, with the robot being controlled by the physician using a joystick [21]. The results of these pilot studies suggested that robotically assisted needle placement for nerve blocks under fluoroscopic guidance is feasible and capable of achieving comparable accuracy to manual techniques [21]. The integration of robotic systems with fluoroscopy aims to leverage the real-time imaging capabilities of fluoroscopy while enhancing the precision and control of interventional procedures, potentially leading to reduced radiation exposure for both patients and medical personnel [21]. While the field of robotic fluoroscopy is still evolving, these examples demonstrate the growing synergy between robotics and real-time X-ray imaging in healthcare [21].

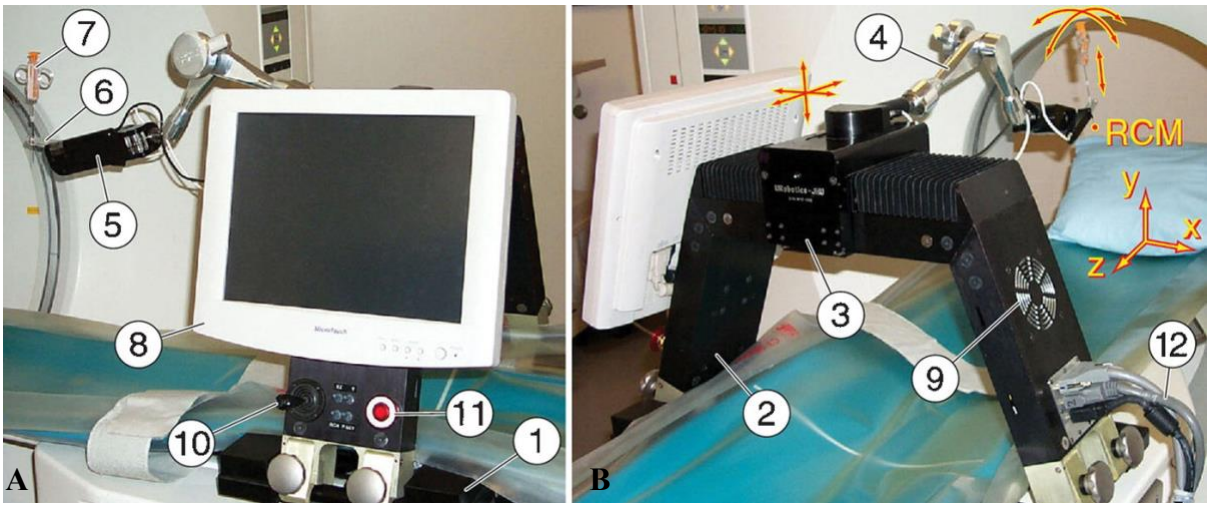


***Figure 10** . **A:** Front view of AcuBot **B:** Lateral view of AcuBot **[21]***

Given the critical nature of medical interventions, thorough testing of such robotic systems is paramount to ensure both their safety and efficacy prior to clinical implementation. The conventional method of repeatedly testing under live fluoroscopy presents a potential risk of unnecessary radiation exposure to the involved researchers. Therefore, the utilisation of a transparent phantom in conjunction with a digital C-arm simulator offers a significantly safer and more controlled means of replicating the fluoroscopic environment for the purpose of device testing, thereby providing a key motivation for the present project.

## Simulation Systems and Phantoms in Fluoroscopic Imaging

Various simulation systems have been developed to replicate X-ray-like imaging for training, procedural planning, and system development. A key technology in this area is the generation of digitally reconstructed radiographs (DRRs), which are simulated X-ray images derived from Computed Tomography (CT) volumes [18,22]. DRRs are essentially perspective volume renderings that simulate the attenuation of virtual X-rays (**Figure 11 Parts A & B**) [22,23]. Different volume rendering techniques exist for DRR generation, including ray-tracing, splatting, shear-warp, and more recently, deep learning-based approaches [22, 24]. While ray-tracing can produce high-quality images, it is computationally intensive [22]. Some cost-effective simulators utilise webcams attached to a miniature C-arm, combined with a semi-transparent phantom, to simulate X-ray images from the webcam videos [22].

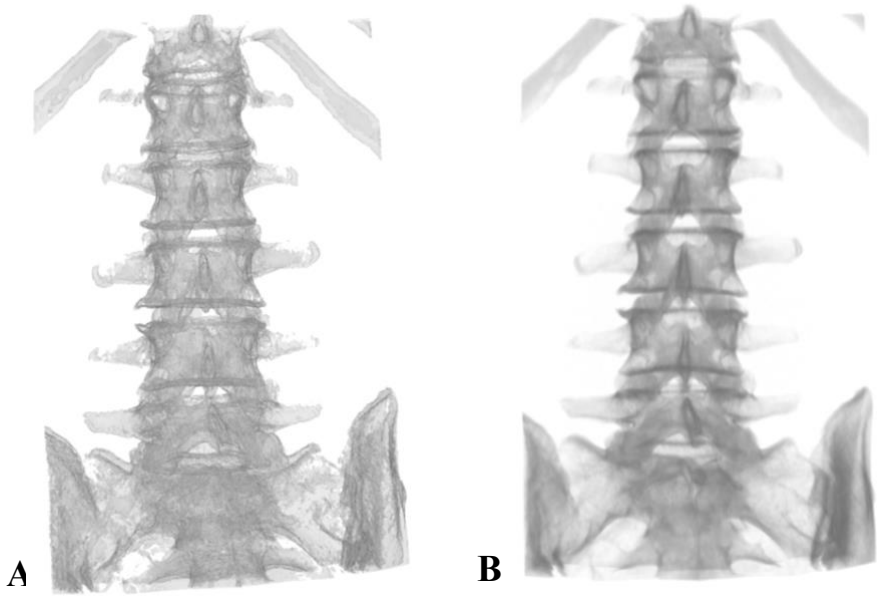


***Figure 11*** *. **(A)** Digitally reconstructed radiographs of spine, **(B)** CT volume of spine used to make the DRR* ***[22]***

C-arm simulators are specifically designed to mimic the functionality of mobile X-ray C-arm systems [22,25]. These simulators function by tracking the position and orientation of a physical or virtual C-arm and generating corresponding DRRs from a pre-loaded CT volume (**Figure 12**) [22]. The primary purpose of C-arm simulators is to provide hands-on training for

clinicians and medical radiation technologists (MRTs) in C-arm manipulation without exposing them or simulated patients to ionising radiation, adhering to the As Low As Reasonably Achievable (ALARA) principle [18]. By allowing users to interact with a physical or virtual C-arm and observe the resulting simulated X-ray images in real-time, these simulators help develop skills in achieving optimal imaging angles for various procedures [22, 25].

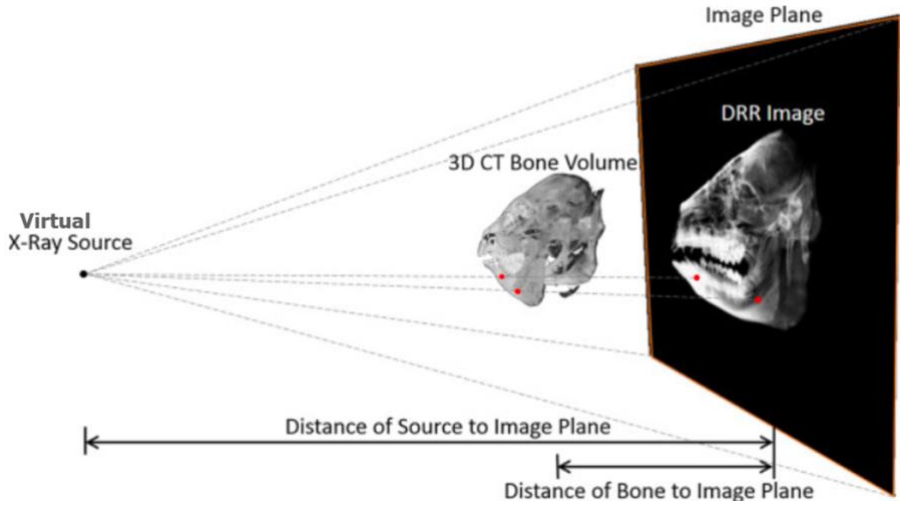


***Figure 12*** *Visual representation of digitally reconstructed radiographs being made from a CT volume* ***[22]***

Different types of C-arm simulators exist, including miniature 3D-printed physical simulators tracked using accelerometers (**Figure 13**) [22], virtual reality (VR) simulators utilising head-mounted displays (HMDs) and hand controllers [22], and computer-based simulators where a 3D model of a C-arm is manipulated on a 2D display [22, 25]. These simulators are used not only for training purposes but also for procedural planning, allowing the pain management team to preview the C-arm angles required for specific views using a patient's CT scan [22]. Furthermore, they can aid in the development and evaluation of intraoperative guidance systems by providing a platform for testing algorithms and techniques using simulated data [22,24].

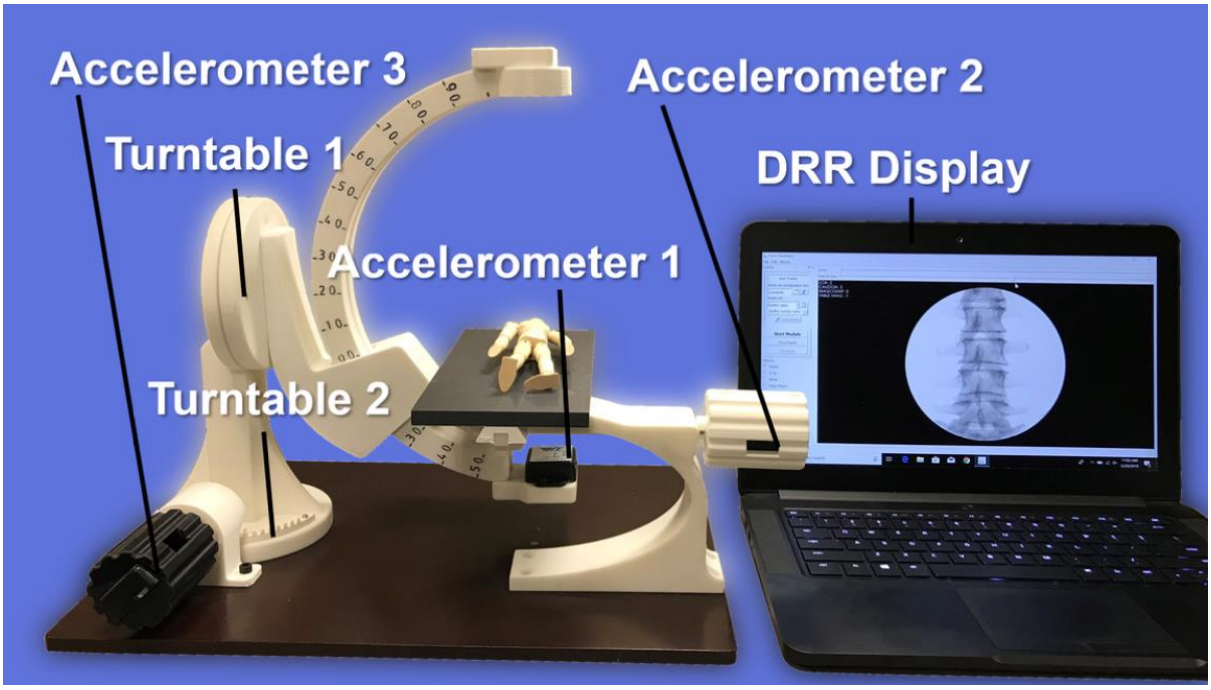


***Figure 13*** *Miniature 3D-printed C-Arm simulator that uses accelerometers to track movement of C-Arm and accordingly update the DRR output.* ***[22]***

Phantoms play a crucial role in both fluoroscopic procedures and related training [22,26,27]. In training, phantoms serve as surrogate patients, allowing trainees to practice procedures such as needle insertion and C-arm positioning in a risk-free and radiation-free environment (**Figure 14**) [22,26,27]. These phantoms can be designed to provide realistic visual and tactile feedback, simulating the texture and resistance of human tissues [27]. Various types of phantoms are used, including physical phantoms made from materials with similar density to bone or soft tissue [27], semi-transparent phantoms for use with webcam-based simulators [22], and even virtual phantoms represented by CT volumes in fully virtual simulators [22]. The application of phantoms extends to the development and calibration of fluoroscopic systems, where they can be used to estimate machine-specific imaging parameters [22]. For instance, calibration phantoms with embedded markers can help establish the spatial relationship between the imaging device and a virtual patient [22]. Overall, phantoms are valuable tools for enhancing training efficacy, reducing radiation exposure, and facilitating the development and evaluation of fluoroscopic imaging technologies [22, 26, 27].

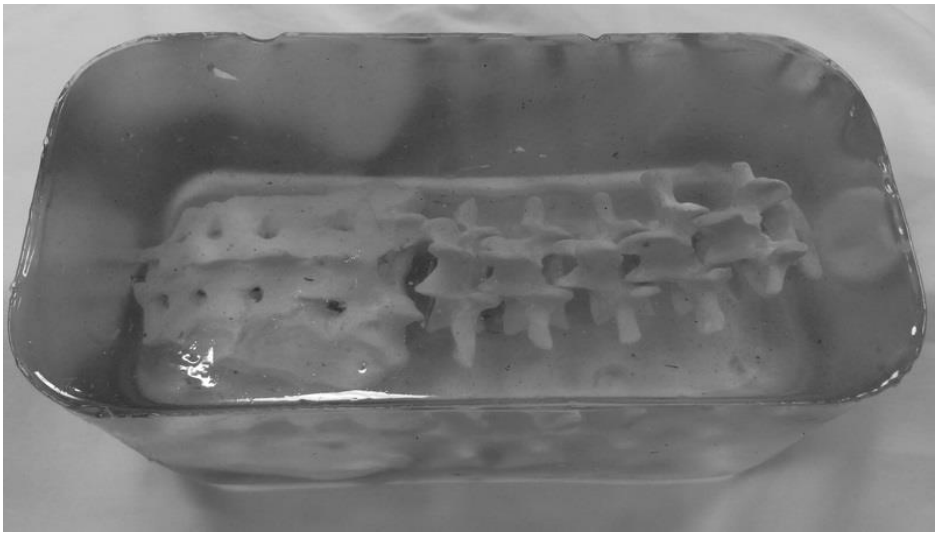

***Figure 14*** *Lumbar Spine phantom for fluoroscopically guided lumbar puncture training* ***[27]***

## 1.3 Digital Imaging and X-ray Simulation Techniques

Digital image processing plays a crucial role in efforts to simulate the visual characteristics of X-ray and fluoroscopic imaging, employing various techniques to mimic the appearance of these modalities. One study investigated the direct capture of X-ray-induced screen fluorescence using a low-cost webcam camera coupled with different shutter sensors [28]. This research aims to develop an affordable digital X-ray imaging system by leveraging cost-effective sensors and assessing the resultant image quality [28]. The method involves varying kV settings of a Philips digital radiography unit and using phototransistor (PH101, BPT1331), photodiode (BPW34), and light-dependent resistor (LDR) sensors to trigger the webcam to capture the visible light produced by a fluorescence screen after X-ray irradiation of an object [28]. Subsequent image processing using the MATLAB application is then employed to analyse the impact of the kV setting on the captured grayscale images, often presenting negative image findings (**Figure 15 Part A**). The quality of the simulated X-ray images is quantitatively assessed by comparing them to images from a Philips DR system using the Mean Squared Error (MSE) value, with lower MSE indicating greater similarity [28]. This webcam-based method, therefore, directly attempts to capture and process the visual output of X-ray interaction to produce a digital analogue, focusing on the relationship between X-ray parameters (like kV) and the resultant digital image characteristics as mediated by different sensor types [28].

Another significant approach to simulating X-ray imaging principles without the use of ionising radiation is optical tomography [29]. This method uses visible light as an analogue to X-rays, employing a divergent and polychromatic LED light source and a USB webcam to capture projections of a semi-transparent object[29]. The system, designed for teaching X-ray computed tomography (CT) concepts, mimics the fundamental principles of CT by acquiring multiple projections of the object at different angles (**Figure 15 Part B**) [29]. A key aspect of

this technique is the characterisation of the visible light source spectrum, acknowledging that different wavelengths experience different attenuations by the sample, analogous to the polychromatic nature of X-ray sources [29]. The captured webcam images, representing the transmitted light through the object, are then processed using computational tomography reconstruction algorithms to generate two-dimensional and three-dimensional tomographic images [29]. While not directly capturing X-ray images, optical tomography effectively simulates the process of projection acquisition and image reconstruction inherent in X-ray CT, using visible light attenuation to represent X-ray absorption and a webcam as a digital detector [29].

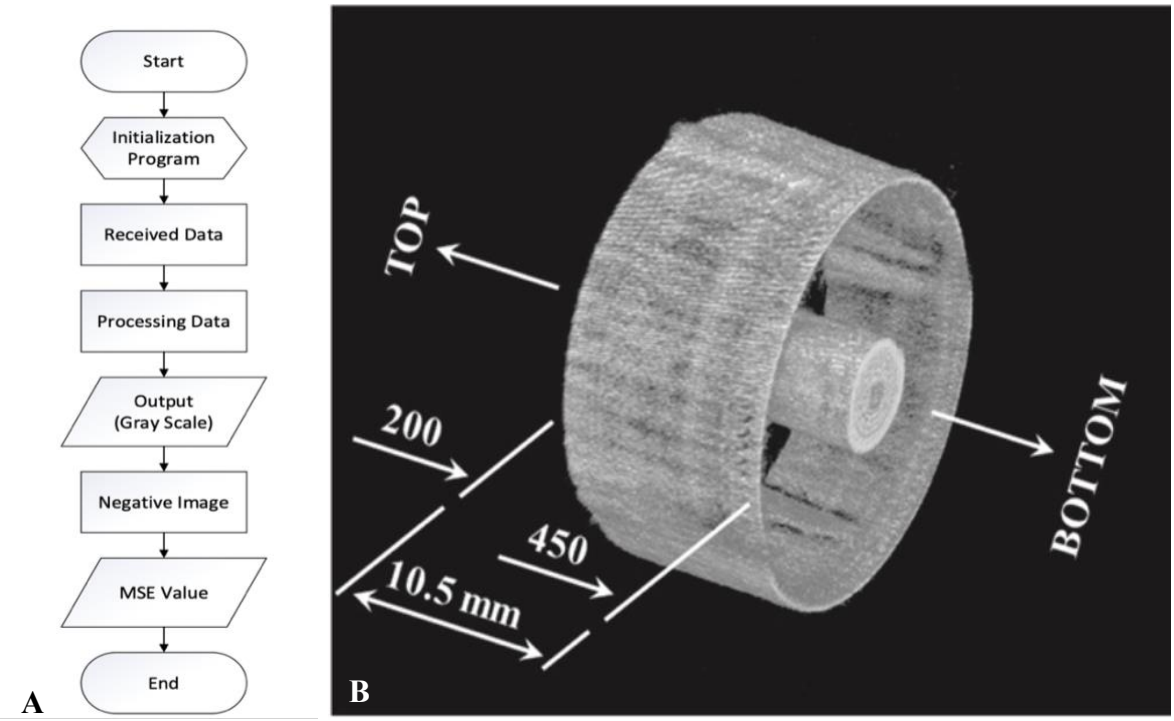


***Figure 15. A:*** *Image processing pipeline used to generate X-ray-like images from a digital camera [28].* ***B:*** *3D reconstructed tomography of the sample from digital images captured from different angles using a rotating webcam [29].*

In contrast to these more direct or analogous simulation methods, another study presented a novel methodology for generating synthetic X-rays from two-dimensional RGB images using conditional generative adversarial networks (CGANs) [30]. This approach, termed pix2xray, employs deep learning to translate an input RGB image into a corresponding synthetic X-ray

image [30]. The method involves training a CGAN on a custom-generated synthetic dataset consisting of RGB images of hand poses, corresponding pose images, and their simulated X-ray counterparts, which are created using a GPU-based ray-tracing software [30]. The pix2xray architecture expands upon a general-purpose image-to-image translation network (pix2pix) by incorporating the hand pose information to improve the accuracy and clarity of the generated X-ray images, particularly in cases with occlusion (**Figure 16 Parts A & B**) [30]. While this method does not rely on direct X-ray capture or an optical analogy, it leverages the power of machine learning to learn the complex mapping between visual features in an RGB image and the expected appearance of an X-ray image of the same subject [30]. The success of this approach is evaluated using image similarity metrics, demonstrating its ability to produce visually plausible synthetic X-rays from standard 2D images, albeit with a different underlying mechanism compared to the webcam-based and optical tomography techniques[30].

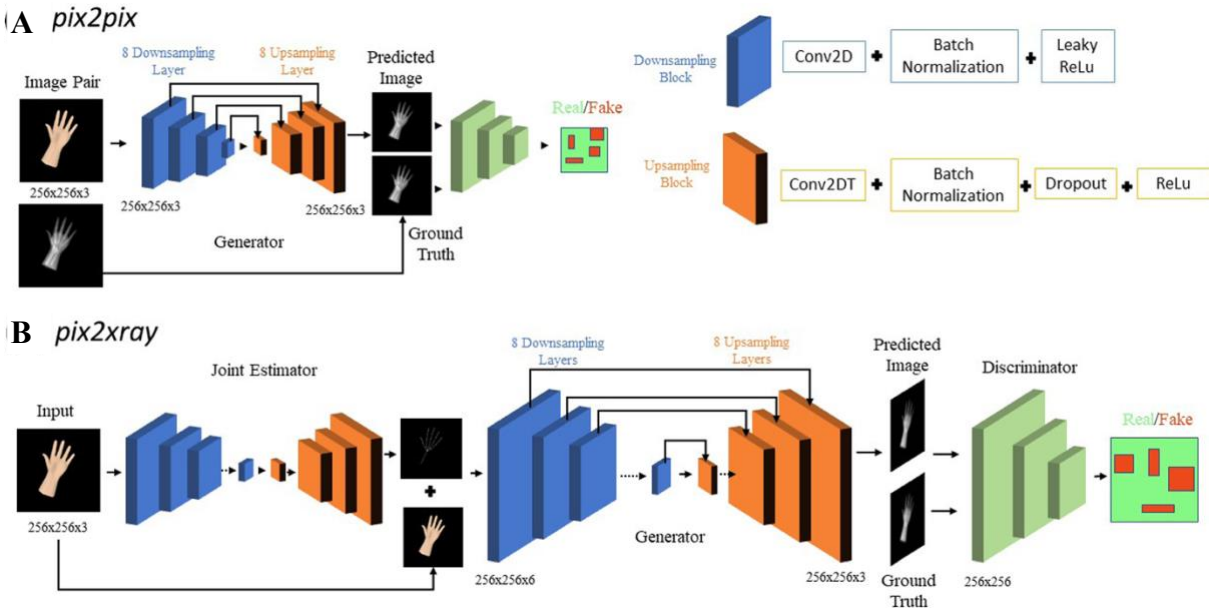


***Figure 16*** *Network architecture overview of* ***A:*** *pix2pix,* ***B:*** *pix2xray* ***[30]***

## 1.4 Hardware Background

Computer-Aided Design (CAD) software is a fundamental tool in modern engineering, facilitating the creation, modification, analysis, and optimisation of designs through the use of computer systems [31]. CAD enables the generation of precise geometric representations in both two-dimensional and three-dimensional space, encompassing curves, surfaces, and solid models [31]. These digital models serve as the essential foundation for subsequent manufacturing processes [31]. While the specific CAD software employed in this project is Fusion 360, its function aligns with the commercially available CAD systems described, which are built around geometric modelling kernels to provide robust solid and surface modelling features [31]. The digital output from CAD software is crucial for driving manufacturing operations such as 3D printing and laser cutting, ensuring the accurate translation of the intended design into physical components [31]. The initial design phase of this project relied heavily on the capabilities of CAD to create the intricate geometries required for various components, providing the necessary digital blueprints for their fabrication.

Embedded control systems are critical for the automation and management of electromechanical systems, enabling them to interact with their environment through sensors and actuators. Microcontroller platforms, such as Arduino, offer a versatile and cost-effective solution for implementing embedded control in a wide range of projects [32]. The Arduino platform, built upon open-source hardware and software, utilises microprocessors like the Atmel ATmega 2560 AVR (**Figure 17**), which can be programmed using languages such as C to create custom control logic [32]. This allows for the development of systems that can respond to both digital and analogue inputs and generate various forms of output, including the control of motors and other electromechanical components [32]. In this project, Arduino microprocessors were selected to provide the necessary computational intelligence for

controlling the actuation of mechanical elements and managing the overall system behaviour based on pre-defined algorithms and sensor feedback. The accessibility and extensive community support for the Arduino platform facilitated rapid prototyping and iterative development of the control system.

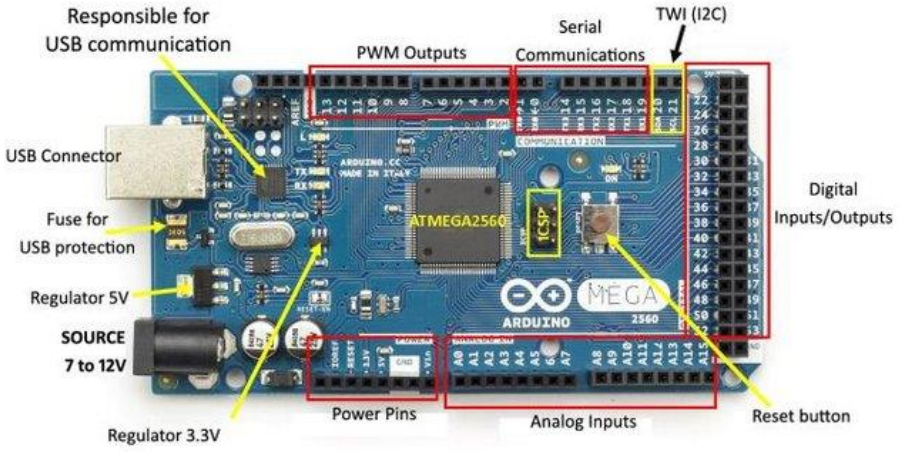


***Figure 17*** *Labelled diagram of commonly used printed circuit board(Arduino Mega 2560) with an ATmega2560 AVR microprocessor* ***[33]***

Stepper motors are a specific type of brushless DC electric motor that are distinguished by their ability to perform precise rotational movements in discrete steps [34]. This characteristic makes them particularly well-suited for applications requiring accurate positioning and controlled motion, such as robotics and automation systems [34]. The operation of a stepper motor involves the conversion of digital pulses into mechanical rotation, with each pulse causing the motor shaft to rotate by a specific step angle (**Figure 18**). To effectively drive and control stepper motors, dedicated electronic circuits known as stepper drivers are essential [34]. These drivers manage the current flow through the motor's windings, allowing for precise control over the energisation sequence of the motor phases, which in turn dictates the direction and speed of rotation. Furthermore, many modern stepper drivers offer micro-stepping capabilities, enabling even finer resolution and smoother motion by dividing each full step into smaller increments [34]. In this project, stepper motors, in conjunction with appropriate drivers, were

employed to achieve the accurate and repeatable mechanical movements required for the functional operation of the designed system.

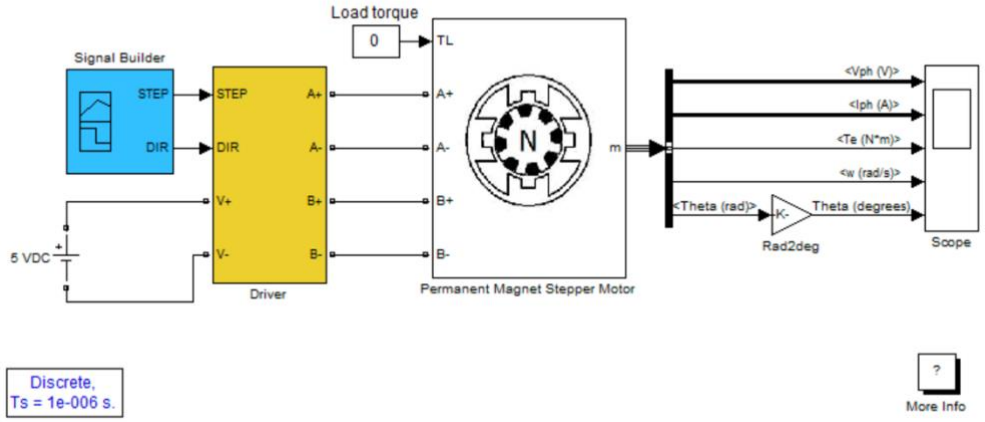


***Figure 18*** *Schematic of a permanent magnet stepper motor system. The setup includes a signal builder generating STEP and DIR signals, a motor driver module, and a permanent magnet stepper motor subjected to a load torque. Outputs such as phase voltage, phase current, electromagnetic torque, angular velocity, and angular position are monitored using a scope.* ***[34]***

## Manufacturing Techniques: $CO_2$ Laser Cutting and 3D Printing with PLA

$CO_2$ laser cutting is an established industrial process that utilises a focused beam of infrared light generated by a carbon dioxide laser to cut a variety of materials, including steel, aluminium, stainless steel, and thermoplastics (**Figure 19**) [35]. The laser beam's energy melts, vaporises, or ablates the material along the intended cutting path, and a pressurised gas, such as nitrogen or oxygen, is often used to expel the molten material and debris from the resulting kerf [35]. This process offers several advantages, including the ability to produce narrow kerf widths, achieve high cutting speeds, and maintain a low heat-affected zone, thereby minimising thermal distortion of the workpiece [35]. $CO_2$ laser cutting is widely employed in manufacturing for creating intricate shapes and precise cuts in sheet materials based on digital designs provided by CAD software [35]. In this project, $CO_2$ laser cutting was utilised to fabricate specific components requiring precise two-dimensional profiles and clean edges, ensuring dimensional accuracy and facilitating subsequent assembly.

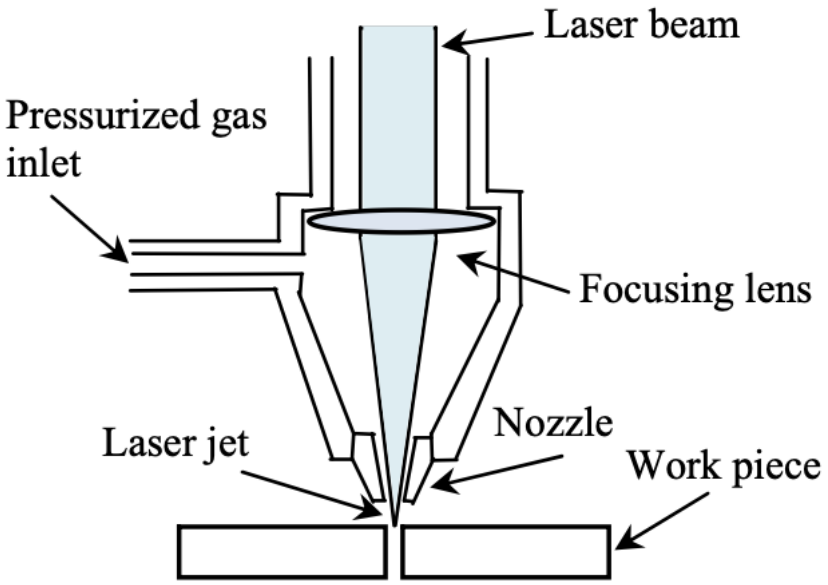


***Figure 19*** *Labelled diagram of the components of a $CO_2$ laser cutter* ***[35]***

Three-dimensional (3D) printing, also known as additive manufacturing, is a technology that builds physical objects layer by layer from a digital model [36]. This process involves the successive addition of material, in contrast to traditional subtractive manufacturing techniques [31,36]. A common and widely used material in 3D printing is Polylactic Acid (PLA), a biodegradable thermoplastic polymer [36]. One prevalent method for 3D printing with PLA is Fused Deposition Modelling (FDM), where a filament of PLA is heated to a semi-liquid state and extruded through a moving nozzle. The extruded material is deposited layer by layer, following the cross-sectional contours of the digital design, and solidifies upon cooling, bonding with the preceding layer to form the final three-dimensional object [36]. PLA is favoured for its ease of printing, relatively low cost, and suitability for a broad spectrum of applications, from rapid prototyping to the production of functional parts with complex geometries [36]. In this project, 3D printing with basic PLA filament via FDM was employed to create components with intricate three-dimensional shapes and internal features that would be challenging or impossible to manufacture using conventional methods. The versatility and accessibility of PLA-based 3D printing allowed for rapid iteration and customisation of various elements within the overall design.

## 1.5 Aims and Objectives

The aim of this project was to develop a radiation-free, webcam-based C-arm simulator capable of generating fluoroscopy-like images of transparent phantoms using visible light and real-time image processing, to support safe, cost-effective surgical training and experimental imaging system development.

The main objectives were:

- Design and construct a modular physical simulator with integrated webcam and motorised control
- Develop a real-time image processing pipeline to replicate fluoroscopy-style imaging using visible light
- Evaluate image quality across multiple lighting configurations and anatomical views
- Validate system usability and realism through expert feedback via a structured questionnaire

**Project Significance**

In recent years, the demand for accessible, low-cost medical training tools has increased, particularly in regions with limited access to conventional imaging equipment. Traditional C-arm systems rely on expensive, radiation-based technologies that introduce financial and safety challenges. This project addresses these barriers by developing a radiation-free simulator constructed from consumer-grade electronics, 3D-printed components, and laser-cut materials. Using visible light imaging and standard fabrication methods significantly reduces costs compared to clinical fluoroscopy systems. Beyond affordability, the modular design supports sustainability and ethical research practices by extending the system's operational lifespan and reducing electronic waste.

# 2. Methodology

## 2.1 Initial Prototyping and Component Sourcing

**Mechanical and Electrical System Upgrades**

The initial stage involved sourcing upgraded mechanical and electrical components to meet the revised design requirements. A key change was the replacement of the NEMA 17 stepper motor, which lacked sufficient torque, with a more powerful NEMA 23 motor for stable operation. To accommodate this, a 10 mm diameter stainless steel shaft was selected to drive the rotational module, along with a compatible timing belt pulley with a 10 mm bore. The structural frame was strengthened by replacing the original 5 mm acrylic plates with 8 mm Perspex sheets, improving overall stability and load-bearing capacity. These changes required the use of longer M5 bolts and screws to secure the thicker materials. A full breakdown of component costs is provided in Appendix D

On the electrical side, solid core wires were chosen for consistent connections to minimise connection errors and improve long-term reliability, and JST connectors were introduced to allow modular plug-and-play interfacing between motors and the control system. An Arduino-compatible shield was used to manage the increasing number of connections in an organised and secure manner, improving wiring layout and maintainability during prototyping and future testing.

**Modular Assembly Design in Fusion 360**

With upgraded components finalised, a complete mechanical redesign was carried out in Autodesk Fusion 360. The simulator was modelled around two key assemblies: the rotating

module, which houses the C-arm and enables cranial–caudal angulation, and the support module, which enables left–right angulation using the upgraded stepper motor.

The rotating module underwent substantial optimisation. Its dimensions were reduced from 200 mm × 100 mm × 65 mm to 120 mm × 66 mm × 61 mm, resulting in a 62.8% volume reduction (**Figure 20 Parts A-F**). This was achieved by repositioning motor mounts and bearing housings closer together and minimising internal empty space. Adjustable linear slots were introduced at critical mounting points, particularly around the motor brackets and bearing seats, to allow flexible placement and fine-tuning during assembly. The redesigned support module was scaled to accommodate the larger NEMA 23 motor, wider timing belt, and 10 mm shaft. All redesigned parts were modelled in Fusion 360 and fabricated using fused deposition modelling (FDM) 3D printing. Initial prototypes were printed and assembled to assess the accuracy of component fit and integration between mechanical and electrical systems to minimise dimensional errors before full-scale fabrication.

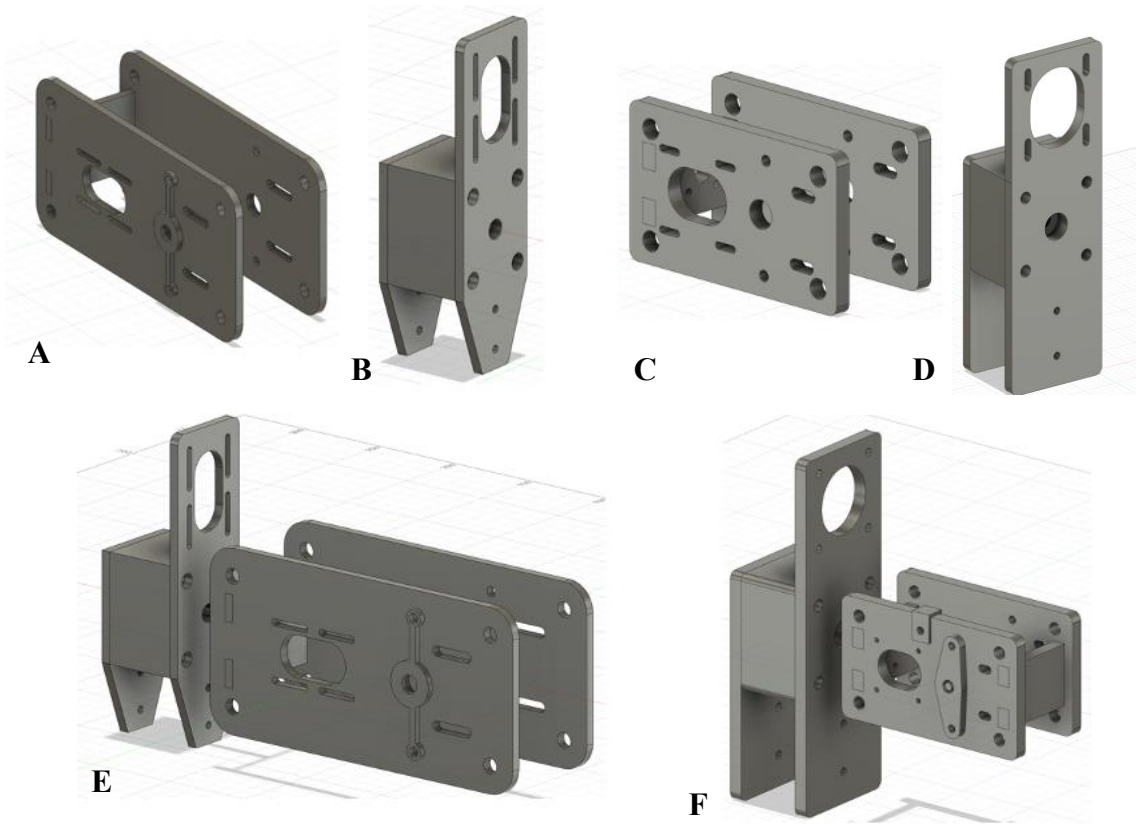


***Figure 20*** *Comparison of original and redesigned components for the C-arm simulator. (**A**) and (**B**) show the initial prototype designs for the rotating and support modules, respectively. (**C**) and (**D**) illustrate the revised versions, featuring a significantly scaled-down and more compact structure. (**E**) shows the fully assembled rotating and support modules from the original prototype, while (**F**) displays the assembled configuration of the redesigned, more compact system.*

**Laser-Cut Acrylic and 3D-Printed Mechanical Parts**

Once the initial mechanical integration and motor testing were validated, final mechanical components were fabricated. Structural elements were manufactured from 8 mm Perspex sheets, laser-cut using pre-generated DXF files exported from Fusion 360. Laser cutting ensured precise, repeatable production of the support module, rotating module, and associated hardware mountings. The acrylic components were assembled using M5 bolts and screws, and fitted with 8 mm and 16 mm bearings as required. Motors and timing belt systems were installed during this phase to verify full mechanical integration.

**Breadboard Prototyping and Stepper Motor Testing**

Following mechanical prototyping, motion control systems were tested using a breadboard setup. Two stepper motors (NEMA 23 and NEMA 17) were connected to independent TB6600 drivers and powered by a 24 V, 15 A regulated DC switching supply (InShareplus, 360 W model). The drivers were connected via breadboards, allowing rapid reconfiguration during testing. An Arduino Mega 2560 board, interfaced with two dual-axis XY joystick modules, enabled manual control of each motor axis independently (**Figure 21**). The primary goal was to verify smooth motor operation, reliable user input response, and enforcement of angular limits. Through experimentation, rotational thresholds of approximately 600 steps were established for each motor, corresponding to the desired cranial–caudal and left–right angulation ranges. Fine adjustments were made to the micro stepping settings on the stepper drivers, improving precision and motion smoothness. Initial motor control code was developed in the Arduino IDE to enable real-time manual control of direction and speed via the joysticks, and included logic for stopping motion at defined limit conditions. This iterative testing phase established a reliable mechanical and electrical foundation for later full-system integration. System testing focused on identifying any unwanted vibrations, mechanical backlash, and

structural weaknesses. The rotating and support modules were mounted to the simulator's base structure, and preliminary movement tests were conducted using the breadboard-driven motor control system. Successful assembly confirmed the structural, mechanical, and electrical compatibility of the revised design, enabling progression toward system integration in subsequent phases.

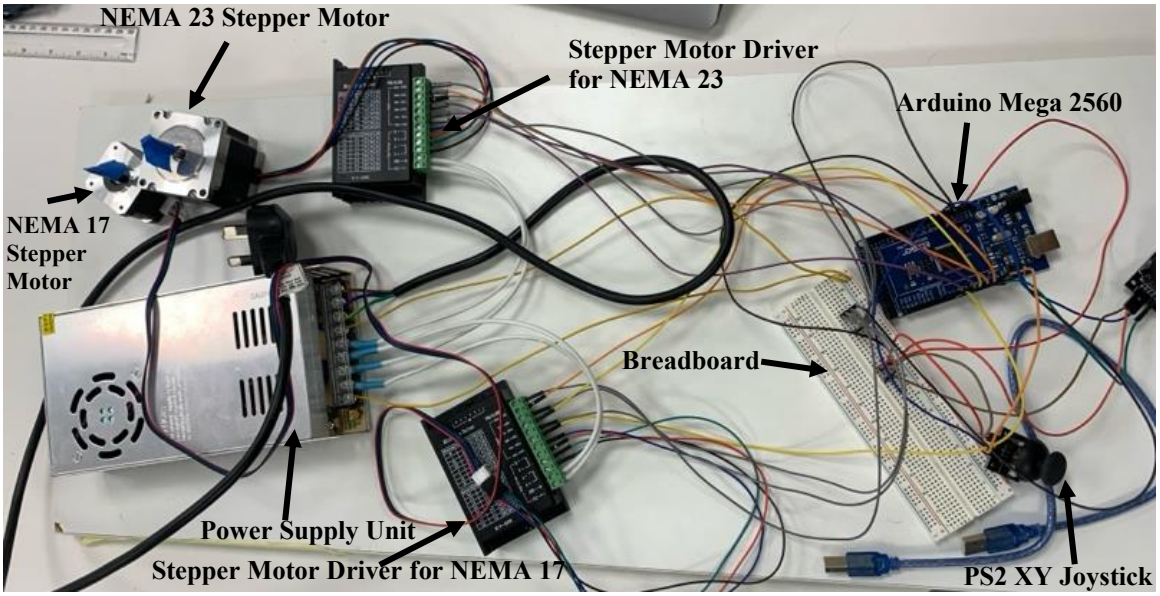


***Figure 21*** *Initial electronic setup for breadboard prototyping of the motion control system. All key components, including the Arduino microcontroller, stepper motor drivers, joystick modules, power supply, and motors, are labelled to illustrate the early-stage configuration used for system testing and development.*

## 2.2 Mechanical Redesign and Assembly Refinement

**Fabrication and Assembly of Initial C-arm**

After completing the rotating module frame, fabrication of the C-arm was undertaken. It was designed as four separate segments in Autodesk Fusion 360 to facilitate printing and assembly. The two central segments, each 238 mm in length, featured gear teeth along their outer arc to engage with the drive gear in the rotating module, allowing ±35° rotational movement (70° total range). The two outer segments, each 375 mm long, were smooth and toothless (**Figure 22 Part A**). All segments were joined using dovetail joints to ensure proper alignment and structural stability (**Figure 22 Parts B**). The final C-arm width was 44.5 cm, deliberately 0.5 cm narrower than the 45 cm rotating module to allow free sliding without obstruction. All segments were printed individually using PLA filament on a Creality Ender 3 Max NEO FDM 3D printer and bonded using epoxy glue, creating a continuous arc structure. This segmented approach accommodated the limited build volume of the printer while enabling modularity during assembly and testing.

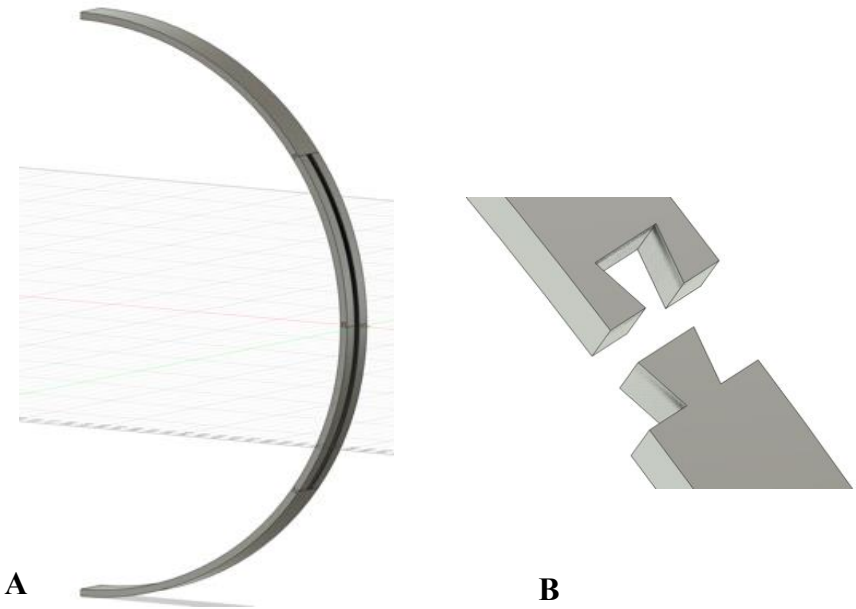


***Figure 22 A:*** *C-arm assembled from four separate segments, with the two central parts containing gear teeth.* ***B:*** *Detail of the dovetail joints used to connect the segments.*

Eight 8 mm diameter bearings, four mounted on each side of the rotating module, supported the C-arm. These provided both contact force to support the C-arm's weight and a low-friction guide for smooth movement. The gear teeth on the central arc interfaced with a steel drive gear mounted on a shaft driven by the stepper motor, completing the motion transmission system. After installation, the C-arm was tested for mechanical compatibility, gear engagement, and rotational freedom, enabling live fluoroscopic angulation without the use of ionising radiation.

**Refinement of Gear Engagement and Belt Drive Mechanism**

Initial testing revealed motion-related issues, notably inconsistent engagement between the drive gear and the C-arm gear teeth. Misalignment arose due to the adjustable slots originally used to mount the bearings, causing occasional gear slippage during rotation. To address this, adjustable slots were replaced with fixed-position bearing mounts in Fusion 360, ensuring consistent alignment and preventing movement during actuation. This resolved the gear engagement issues.

A separate problem was identified with the timing belt system. The short distance between the stepper motor and output shaft made sourcing a suitable standard timing belt difficult. A custom belt tensioner was designed by introducing a third idler pulley above the motor and output shaft pulleys, forming a triangular belt path (**Figure 23 Part A)**. However, passive tensioning was insufficient. To solve this, a 3D-printed sliding bracket was fabricated to allow vertical adjustment of the idler pulley, enabling manual belt tightening (**Figure 23 Parts B-E**). Once tensioned, a spacer piece was inserted beneath the bracket to lock it into position to minimise belt slack and maxim torque transmission . This solution allowed fine-tuning of belt tension while maintaining compactness, and subsequent tests confirmed reliable torque transmission without belt slack. These refinements transitioned the mechanical system from early-stage prototyping toward a more stable, production-ready configuration.

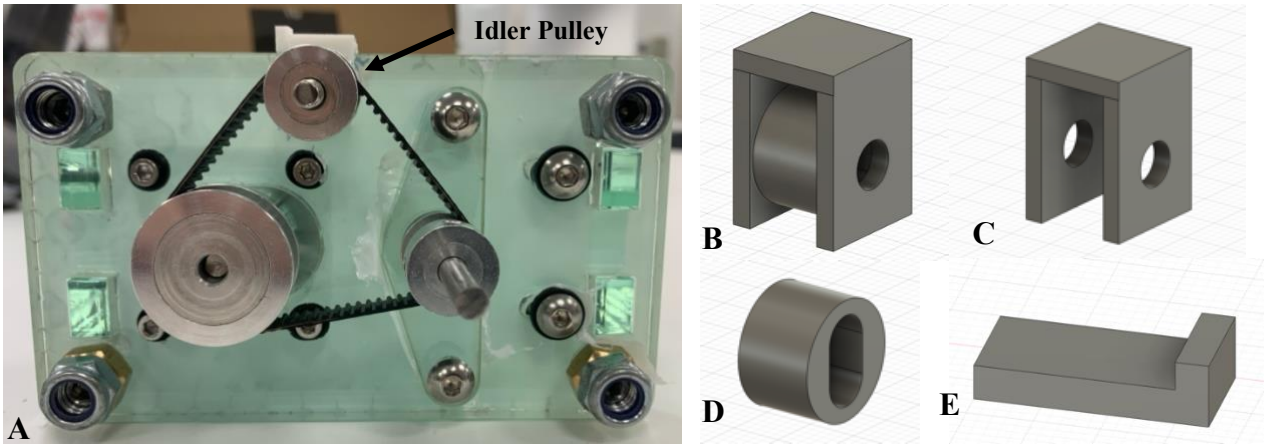


***Figure 23 A:*** *Completed belt tensioning system with the idler pulley labelled.* ***B:*** *Sliding bracket fully assembled.* ***C*** *and* ***D:*** *Individual components of the sliding bracket.* ***E:*** *Spacer used to lock the sliding bracket in position after tension adjustment.*

## Fabrication and Assembly of Revised C-arm

Further testing exposed mechanical wear in the original four-part C-arm design. Over time, adhesive fatigue and mechanical stress at the midline dovetail joint between the two central, geared segments led to gear profile discontinuity, causing skipping, stalling, and jamming.

To eliminate this failure point, a revised central segment was designed to be printed as a single continuous part containing the full gear arc (**Figure 24 Part A**). Due to its size, this component was fabricated using a larger-format Anycubic Chiron 3D printer with basic PLA filament (**Figure 24 Part B**). Surface artefacts were removed via sanding and fine filing to optimise gear smoothness. The remaining two outer segments were printed separately using the Creality Ender 3 Max NEO and bonded to the central segment using epoxy adhesive, forming a final three-piece C-arm structure.

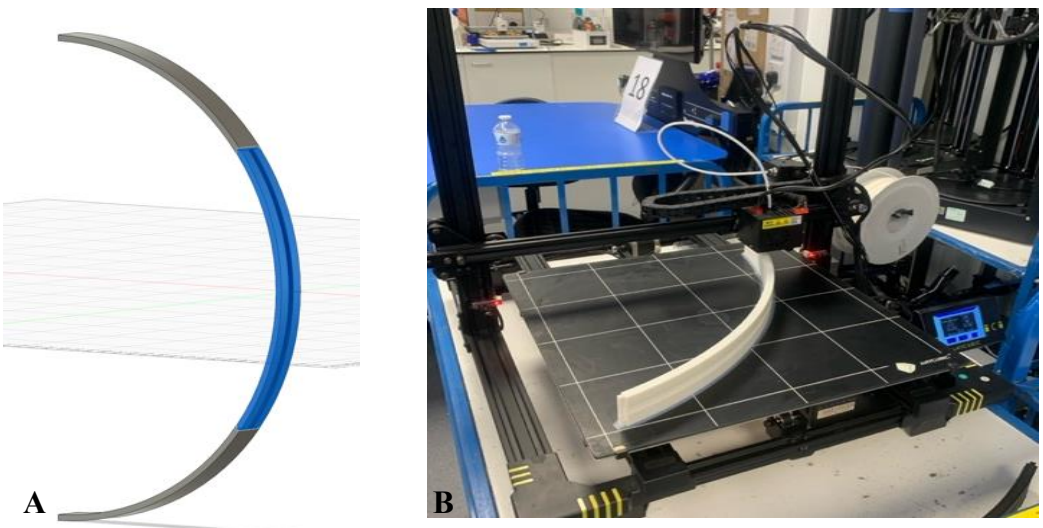


***Figure 24 A:*** *Revised C-arm with a single-piece central segment containing the full gear profile.*
***B:*** *Printing of the continuous geared segment on the Anycubic Chiron 3D printer.*

This redesign eliminated the midline gear discontinuity, restoring consistent, smooth rotational motion without skipping or jamming, and significantly improving overall system reliability.

## Initial Motor Code Development and Testing

Early-stage motor control code was developed using the Arduino IDE to drive the two stepper motors responsible for C-arm movement (**Appendix B**) . Two dual-axis joysticks allowed independent manual control of cranial–caudal and left–right angulations. Joystick input was mapped to enable ±35° cranial–caudal rotation (70° total) and ±90° left–right rotation (180° total). Movement limits were enforced based on calculated motor step counts, factoring in micro stepping (set to 1/16) and the gear ratios. A "dead zone" was programmed around the joystick centre to prevent unintended motion from small accidental inputs. Each joystick's integrated push-button triggered a return to the neutral position (0°) for the respective axis, aligning the C-arm back to the anatomical AP (anterior–posterior) orientation.

Testing confirmed that the joystick-based manual control system provided smooth, responsive motion without excessive vibrations or mechanical instability. This validated both the hardware–software interface and the feasibility of real-time C-arm manipulation using manual controls.

# 2.3 Control Interface and Electrical System Integration

**Soldering and Housing Electronic Components**

Following mechanical and motor validation, focus shifted to upgrading the control system and enclosing the electronics to improve durability, safety, and usability. Breadboard-based connections were replaced with permanent soldered wiring. Solid core 22-gauge wires were soldered directly onto a custom Arduino-compatible shield mounted on an Arduino Mega 2560 board, maintaining a compact vertical assembly and reducing connection instability (**Figure 25** ).

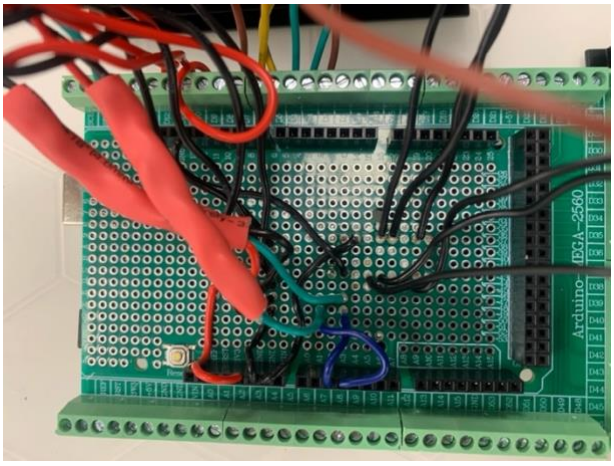

***Figure 25*** *Soldered electronic connections onto an Arduino-compatible prototyping shield mounted on an Arduino Mega 2560 board.*

A custom 3D-printed baseplate was designed in Fusion 360 to securely house all major electronic components (**Figure 26**). The baseplate incorporated moulds for the two stepper motor drivers, the Arduino Mega 2560, and power distribution elements. Once installed, the baseplate filled the internal enclosure footprint, preventing lateral movement of components during transport and operation.

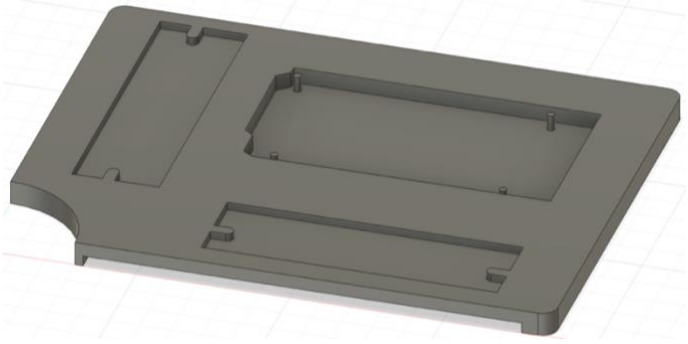

***Figure 26*** *CAD model of a custom-designed mounting plate to secure the stepper motor drivers and Arduino Mega 2560 inside the electrical enclosure, preventing internal movement during transport and operation.*

## Joystick and Push Button Interface Implementation

The joystick system was upgraded from a dual-joystick prototype to a four-axis potentiometer joystick (Bzocio D300B-R4, 10 kΩ resistance), capable of controlling both cranial–caudal and left–right movements through perpendicular analogue inputs. Since this joystick lacked an integrated push-button, four external tactile push buttons were added and hardwired to the Arduino system (**Figure 27**) . All joystick and push-button connections used solid core wiring, with JST connectors added where modular disconnection was necessary. In particular, the NEMA 23 motor was fitted with custom JST connectors to allow rapid detachment without opening the electronics enclosure, while the NEMA 17 motor retained its original ribbon cable.

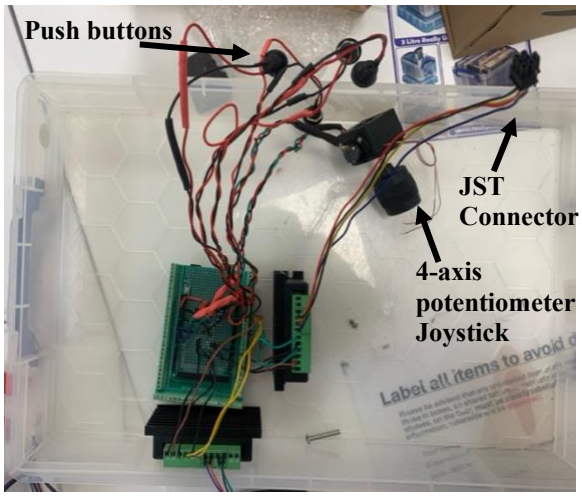


***Figure 27*** *Main electronic components including the four push buttons and joystick module soldered to the Arduino Mega 2560 system.*

The four push buttons were programmed to trigger nine preset fluoroscopic positions using single-click, double-click, and triple-click logic. Button 1 controlled RAO angles, Button 2 LAO angles, Button 3 cranial and caudal tilt, and Button 4 served as a reset and lateral view selector. A software-based debounce delay was implemented to avoid accidental multi-click misinterpretation. EEPROM memory was used to track the real-time angular position of each motor to minimise cumulative positioning errors during multiple movements , ensuring that preset movements were executed relative to the current C-arm position rather than assuming a neutral start. For instance, if the system was positioned at LAO 30° and commanded to move

to RAO 30°, the motors would calculate and perform a 60° transition, preserving positional continuity. Manual joystick adjustment remained available for fine positioning, and the live angular displacement was output to the Arduino serial monitor for calibration and validation. to validate motor calibration and minimise step count errors.

## Electronics Housing Design and Assembly

A dedicated enclosure was designed in Fusion 360 to house the joystick and push buttons, providing internal cable management routes and a clean external layout (**Figure 28 Parts A&B**). The housing was labelled with KCL branding and mounted adjacent to the main electronics box for convenient user access. All electronic components, including the Arduino Mega 2560, stepper motor drivers, and power distribution were enclosed within a dedicated electrical box (**Figure 28 Part C**). A mains extension cable supplied power to both the Arduino and the motor drivers from a single outlet. No voltage regulation circuitry was required, as all devices were matched to their rated input voltages. The final wiring configuration had only two external outputs: one for the power cable and one for the joystick module. This arrangement allowed simple plug-in operation while ensuring that the internal electronics remained compact, organised, and protected during handling and transportation.

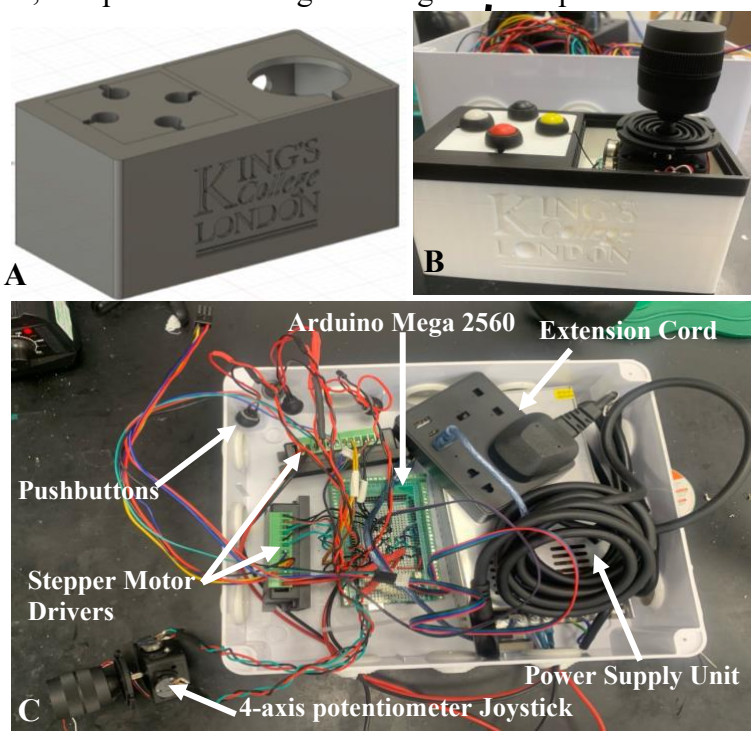


***Figure 28 A:*** *CAD model of the joystick and button housing.* ***B:*** *Printed and assembled housing with joystick and buttons installed.* ***C:*** *Complete electrical system placed inside the electrical enclosure.*

# 2.4 Digital Imaging Processing Pipeline and Lighting

**Development of Real-Time Image Processing Pipeline**

The fourth phase focused on creating a real-time image processing pipeline written in Python to transform visible-light video into a fluoroscopy-style output (**Figure 29**)(**Appendix C**). A wireless webcam (Toallin Wireless 1080p Webcam) was used as the primary image acquisition device. Initial development involved applying grayscale conversion, image inversion, and edge detection to the raw video feed. Both Sobel and Canny edge detection algorithms were trialled. Although the Canny filter produced cleaner contours, the Sobel method was selected for its stronger sensitivity to the subtle gradients typical of semi-transparent phantom materials. After edge detection, the processed image was inverted and horizontally flipped to replicate the standard viewing orientation seen in fluoroscopy.

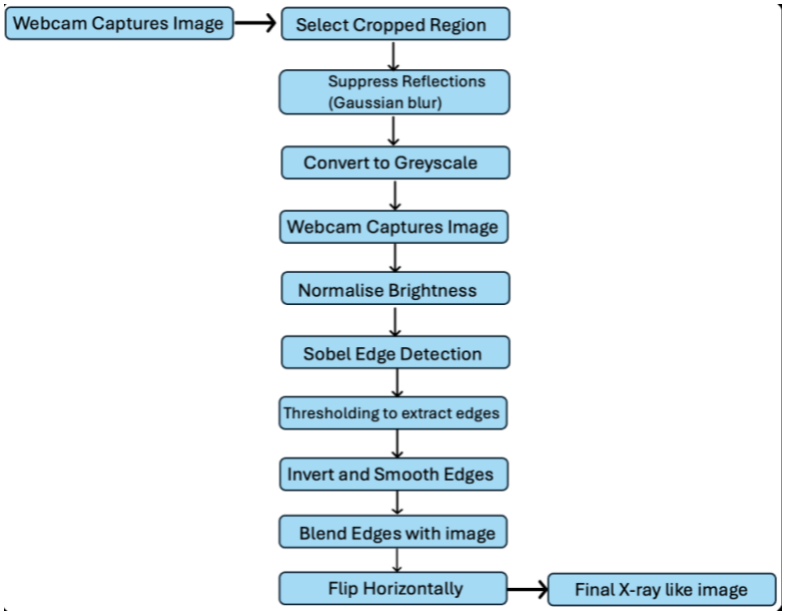


***Figure 29*** *Flowchart showing digital image processing pipeline used to achieve fluoroscopic effect*

To focus on relevant structures, a region-of-interest (ROI) cropping feature was added, allowing users to select a specific imaging area and exclude environmental noise captured by the wide-angle webcam (**Figure 30 Parts A & B**). Gaussian blurring was also incorporated into the pipeline to minimise the effect of surface glare and lighting artefacts. These pre-

processing steps optimised the clarity and realism of the final output while maintaining the system's ability to run in real time.

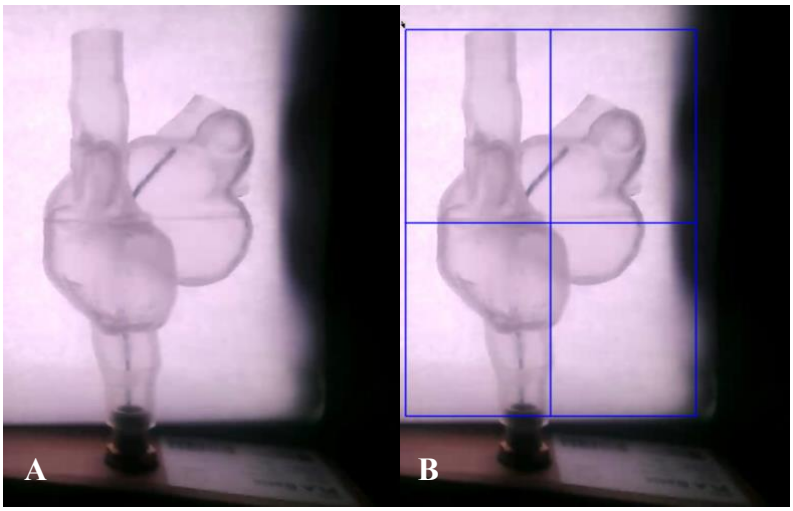


***Figure 30 A:*** *Preview of the webcam feed before selecting the Region of Interest (ROI).*
***B:*** *Region of Interest selected around the phantom, indicated by blue boundary lines.*

## Testing Various Light Sources and Image Calibration

After establishing basic image processing functionality, the next step was optimising the lighting conditions to enhance phantom visibility. Two main illumination strategies were evaluated. The first setup used a broad, diffused backlight created by positioning a rectangular light pad behind the phantom (**Figure 31 Part A**). To soften excessive brightness and mimic clinical X-ray contrast, a paper diffuser was placed in front of the light source. This produced clear silhouette images, ideal for edge detection.

The second approach involved using a Proxinova 150-lumen wireless floodlight placed on the C-Arm opposite to the camera which provides a mobile light source that adjusts to the C-arm movement, always keeping the phantom in the centre (**Figure 31 Part B**). Again, a paper diffuser was employed to spread the illumination evenly across the phantom. Both lighting setups were tested under controlled conditions, and image processing parameters such as thresholding and blurring were fine-tuned accordingly to compensate for variations in brightness and edge clarity.

To further minimise glare from the transparent phantom surfaces, a linear polarising film was mounted over the webcam lens. This significantly reduced surface reflections, improving the consistency of detected edges across different lighting scenarios. Additional tests were conducted within a fully enclosed cabinet to eliminate ambient light interference, ensuring that only the intended backlighting contributed to the captured images. This setup provided more consistent thresholding and enhanced the visibility of low-contrast features within the phantom. The final system combined real-time video acquisition with effective lighting control, polarisation strategies, and an optimised image processing pipeline. This integration successfully produced fluoroscopy-style images suitable for live phantom manipulation and catheter training simulations without the use of ionising radiation.

.

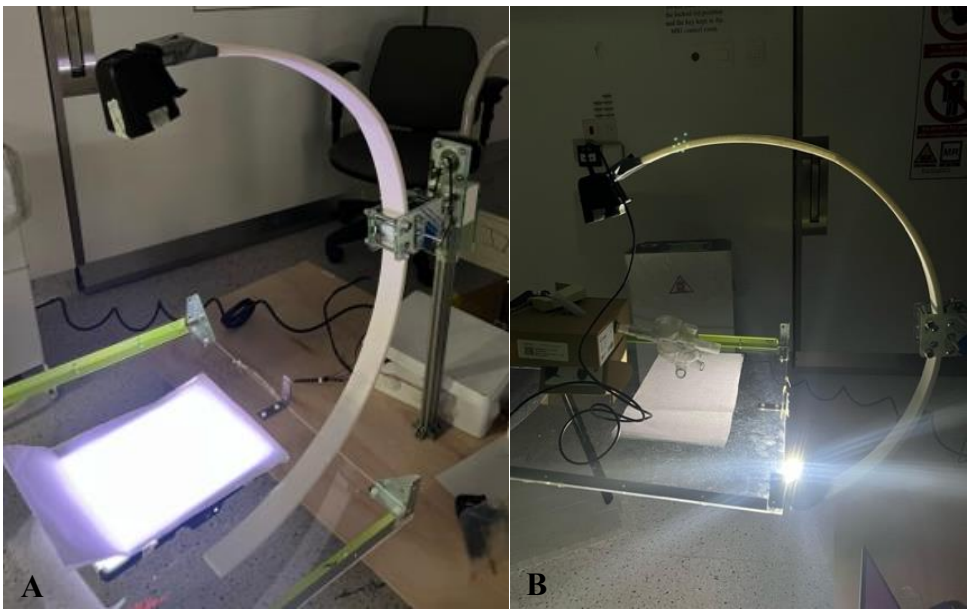


***Figure 31 A:*** *Imaging setup using a diffused backlight placed behind the phantom.*
***B:*** *Imaging setup using a dynamic floodlight mounted on the C-arm, moving together with the rotating module.*

## 2.5 Final Assembly and Experimental Setup

**Assembling and Mounting Simulator onto Wooden Platform**

The final phase of development involved the full mechanical assembly of the simulator and the construction of a stable experimental platform to validate system performance. The rotating module was mounted onto the support module, which incorporated two pre-cut slots designed to accommodate aluminium extrusions (2040T profile, dimensions 500 mm × 40 mm × 20 mm). A pair of extrusions were inserted and secured into these cutouts to provide vertical support rails for the simulator. These extrusions were then fixed to a 9 mm thick plywood base measuring 1250 mm by 650 mm using eight angle brackets, which were bolted through both the extrusions and the base to ensure stability and rigidity (**Figure 32**).

The electronics housing, containing the Arduino Mega 2560 microcontroller, stepper motor drivers, and power distribution components, was positioned behind the rotating module. Wiring was routed neatly to minimise clutter and reduce mechanical strain on connectors. A single mains extension cable was led out of the enclosure, supplying power to the Arduino system and motor drivers from a common outlet. To enhance portability, the entire assembly was mounted onto a mobile trolley, allowing the simulator to be transported easily between testing locations without compromising structural integrity.

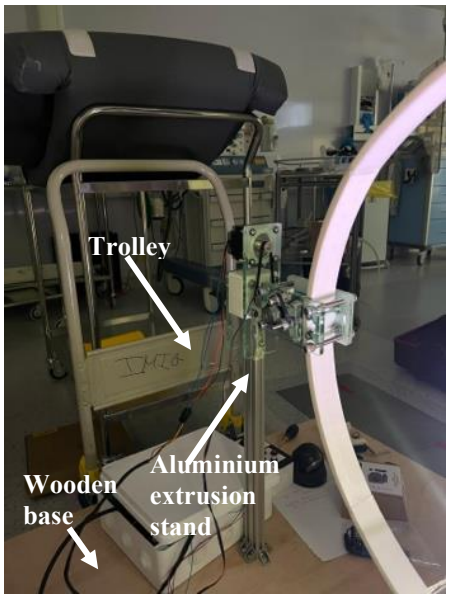




***Figure 32*** *Final mechanical assembly of the simulator, showing the aluminium extrusion stand and the wooden base, with key structural components highlighted.*

The webcam used for imaging was attached to one side of the C-arm using lightweight duct tape. This attachment method was selected to minimise additional mechanical load and avoid introducing stress that could deform the C-arm structure during motion. To balance the system and replicate the standard X-ray C-arm configuration, the floodlight was affixed to the opposite side of the C-arm. This arrangement ensured that the phantom was positioned centrally between the light source and the imaging device, maintaining a geometry consistent with clinical fluoroscopic imaging systems.

## Phantom Setup and Final Experimentation

To evaluate the simulator's functionality under realistic imaging conditions, a basic phantom experiment was designed. A transparent phantom was placed inside a repurposed cardboard box, originally used for 3D printing filament packaging. A hole was cut into the side of the box to allow for the insertion of the phantom, and a rubber tube was connected to simulate a vascular entry path. This tubing exited through the top of the box, providing access for the controlled insertion and manipulation of a radiofrequency ablation catheter within the phantom (**Figure 33 Parts A-C**).

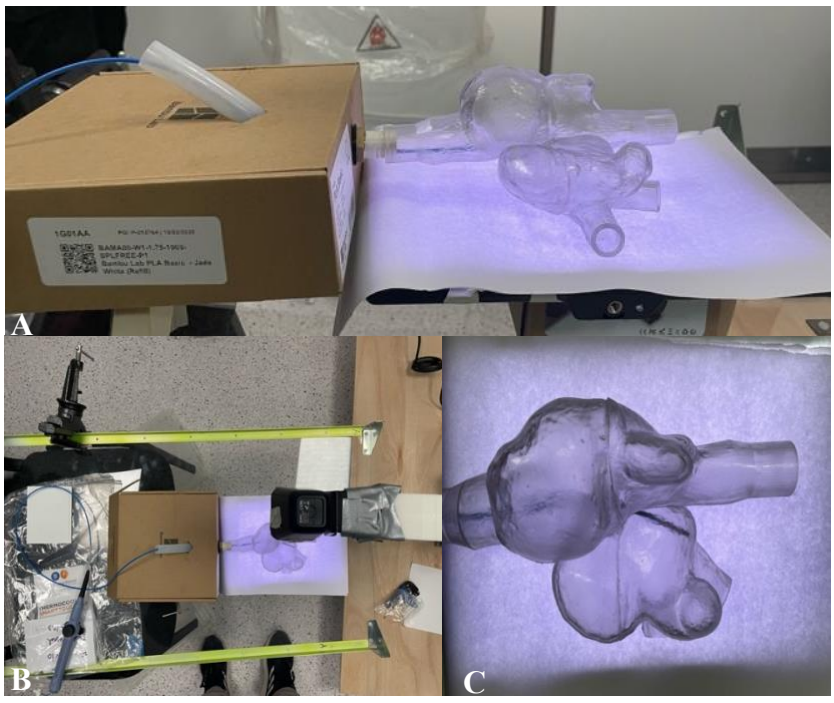


***Figure 33 A:*** *Phantom setup showing catheter insertion into the phantom bed.* ***B:*** *Clear Perspex sheet used as the phantom bed during the experimental setup to allow imaging of the phantom through the base.* ***C:*** *Phantom placed on top of the backlight with diffused paper, with the catheter visible inside the phantom structure.*

During testing, the webcam transmitted a live video feed wirelessly to a laptop running the Python-based image processing pipeline. Using the upgraded joystick and push-button control interface, the user was able to reposition the C-arm through clinically relevant fluoroscopic angles while observing the resulting processed images in real time. This setup enabled the system to emulate the experience of manipulating a live fluoroscopy machine without the use of ionising radiation.

The full system successfully demonstrated real-time fluoroscopy-style imaging for transparent phantoms under dynamic conditions, validating both the mechanical motion control and the digital imaging pipeline. The experimental setup confirmed that the simulator could support procedural training by providing responsive C-arm manipulation and realistic imaging feedback, fulfilling the project's core design objectives.

# 3. Results

## 3.1 Mechanical System Performance

The mechanical system of the simulator was composed of four primary components: the rotating module responsible for cranial–caudal angulation (**Figure 35 Parts A-E**), the support module enabling left–right rotation (**Figure 35 Parts A-C**), the 3D-printed C-arm itself (which housed the camera and light source), and the aluminium extrusion-based base and stand, which provided overall structural integrity (**Figure 36 Part A**). During testing, the complete mechanical assembly exhibited no structural faults, fractures, or systematic failures. The adjustable belt tensioner within the rotating module operated reliably and maintained sufficient tension throughout testing, ensuring smooth and controlled cranial–caudal rotation. The gear teeth along the C-arm arc maintained full engagement with the drive gear with little to no slippage or misalignment (**Figure 36 Part B**). Notably, the system withstood the combined weight of the wireless webcam and floodlight without mechanical strain or evidence of stalling. The aluminium stand, mounted to a plywood base, provided adequate support throughout the experiment. There was no observable wobble, tilt, or tipping, even during full-range motion in both axes. The system remained rigid and stable during actuation, and the load distribution across the base appeared even. No loose fasteners, structural rattling, or vibration-related defects were observed at any point during operation.

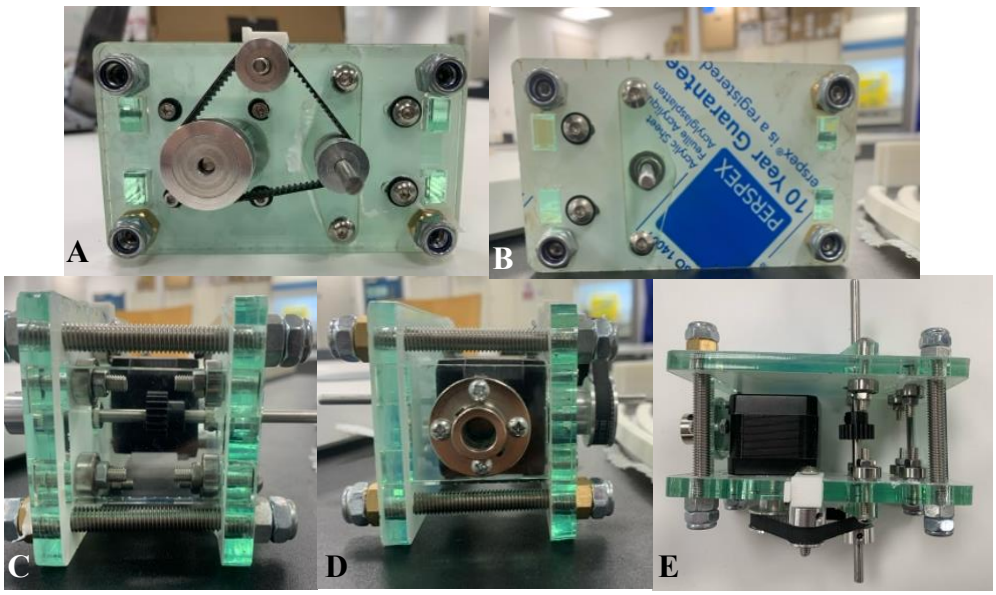


***Figure 34*** *Different views of the rotating module:* ***A:*** *Lateral view showing the belt tensioner mechanism.* ***B:*** *Lateral view from the opposite side.* ***C:*** *Front view.* ***D:*** *Rear view.* ***E:*** *Top-down aerial view.*

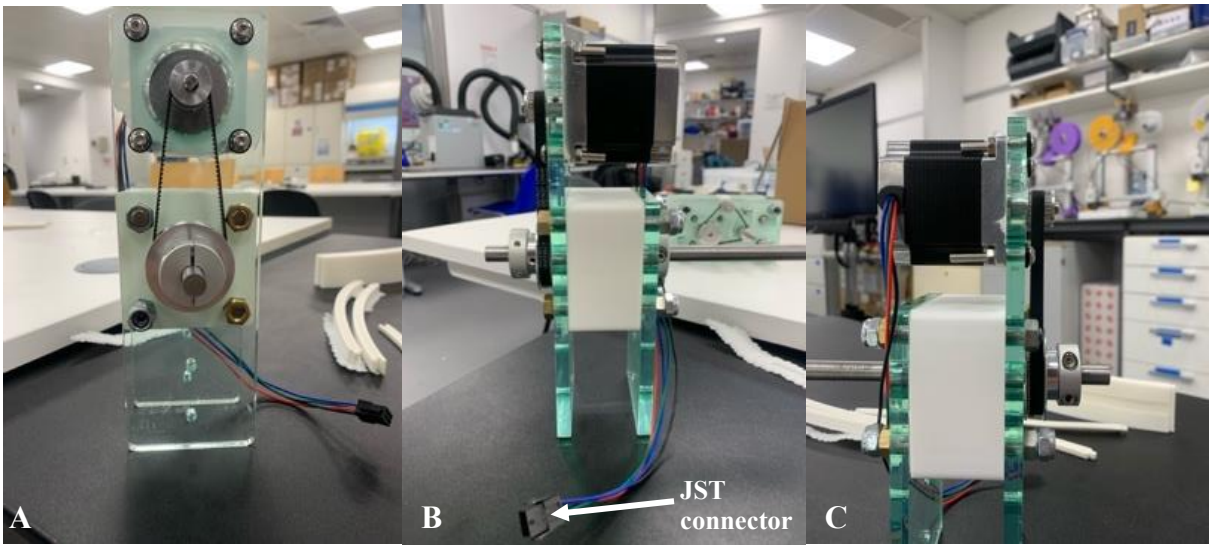


***Figure 35*** *Different views of the support component:* ***A:*** *Front view showing the timing belt pulley.* ***B:*** *Lateral view showing the JST connector.* ***C:*** *Lateral view from the opposite side showing the motor.*

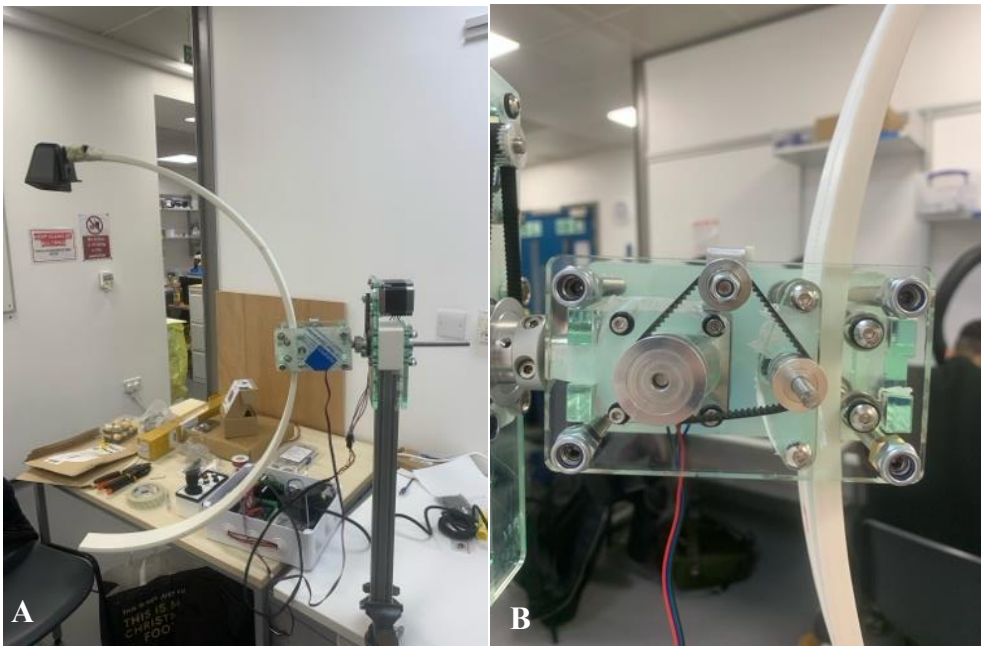


***Figure 36 A:*** *Completed simulator with assembled C-arm rotating module, support component, stand, and integrated camera.* ***B:*** *C-arm positioned within the rotating module, showing engagement with the gear and bearing system.*

| Question | Metric Type | Participant 1 | Participant 2 |
|---|---|---|---|
| Mechanical stability | 1-5 rating | 4 | 3 |
| Vertical smoothness | 1-5 rating | 4 | 4 |
| Rotational smoothness | 1-5 rating | 4 | 4 |
| Resistance issues | Qualitative | No issues | No issues |

***Table 1*** *Results from the Mechanical Performance section of the questionnaire.*

These observations were supported by participant feedback obtained from a structured questionnaire (**Appendix A**) . A biomedical engineers and a senior academic who had previous experience using real C-arm systems evaluated the simulator's mechanical performance. The average rating for mechanical stability was 3.5 out of 5, with smoothness of cranial–caudal movement rated 4 out of 5 by both users. Left–right (rotational) movement also received a consistent rating of 4 out of 5. Both participants reported no mechanical issues (**Table 1**). Overall, the mechanical design was judged to be stable, robust, and effective in supporting the simulator's full range of motion without compromising safety or structural performance.

## 3.2 Electrical System Performance

The electrical subsystem of the C-arm simulator was designed to deliver reliable, responsive control throughout full-range operation. Key components included the stepper motor drivers, power supply unit, control interface (comprising a joystick and multiple tactile buttons) (**Figure 37 Part A**), and the microcontroller and its shielded wiring setup .During testing, the electrical system functioned reliably without interruption or failure. No temperature-related issues were encountered, the motors remained cool throughout extended periods of use, and there was no evidence of overheating in the power supply or control modules. All input mechanisms, including joystick axis detection and push-button activation, registered correctly and without delay. System responsiveness was consistently immediate, with no observable lag, misread inputs, or false triggering. All electrical connections, solder joints, and modular plugs remained intact and stable during both static and dynamic operation.

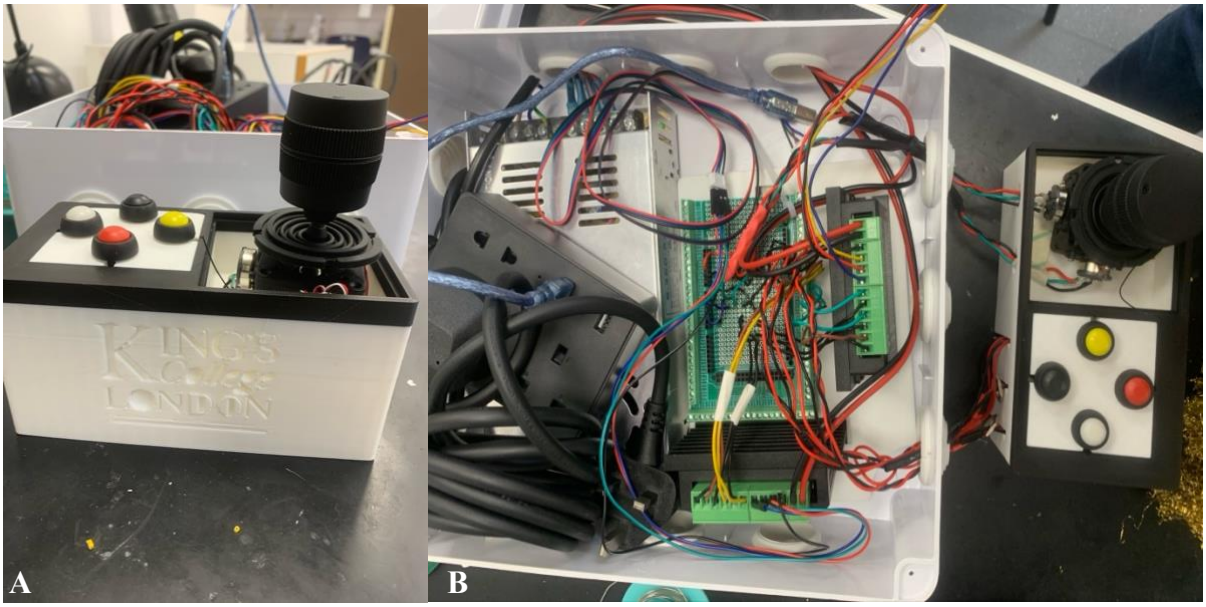


***Figure 37 A:*** *Final electrical component setup with all components placed inside the electronic enclosure, with wires routed into the control module box.* ***B:*** *Highlighted view of the button and joystick box.*

The motors performed precisely in response to user inputs and exhibited no instability, noise, or excess vibrations. The internal electronics were housed in a compact enclosure that maintained both component security and cable organisation (**Figure 37 Part B**). . The design of the enclosure and cable routing ensured easy access for maintenance while maintaining a clean internal layout.

| **Question** | **Metric Type** | **Participant 1** | **Participant 2** |
|---|---|---|---|
| Control responsiveness | 1-5 rating | 5 | 5 |
| Electronics issues | Qualitative | No issues | No issues |
| Wiring organisation | 1-5 rating | 4 | 4 |

***Table 2:*** *Results from the Electrical Performance section of the questionnaire.*

These observations were corroborated by feedback from both participants in the structured evaluation. The responsiveness of the control system was unanimously rated 5 out of 5, with no electronic issues reported by either user. The organisation and accessibility of the wiring and internal layout were also rated 4 out of 5, highlighting the clarity and compactness of the enclosed system (**Table 2**).

Overall, the electrical system was deemed robust, responsive, and user-friendly, contributing significantly to the simulator's overall usability and reliability.

## 3.3 Simulator Image Output Analysis

A resin-printed heart phantom only containing atria and major vascular structures, was used to evaluate the simulator's imaging capabilities. The phantom was first imaged on a clinical low-dose fluoroscopic C-arm across nine standard anatomical views: anterior–posterior (AP), LAO 30°, LAO 60°, left lateral (90°), RAO 30°, RAO 60°, right lateral (90°), cranial 15°, and caudal 15° (**Figure 38 Parts A-I**).. These reference images served as a benchmark for comparing simulator performance. The same phantom was then imaged using the C-arm simulator under two lighting configurations: a diffused backlight and a directional floodlight. Screenshots were taken from a live feed during simulator operation, and a region of interest (ROI) was manually selected at the start of each trial.

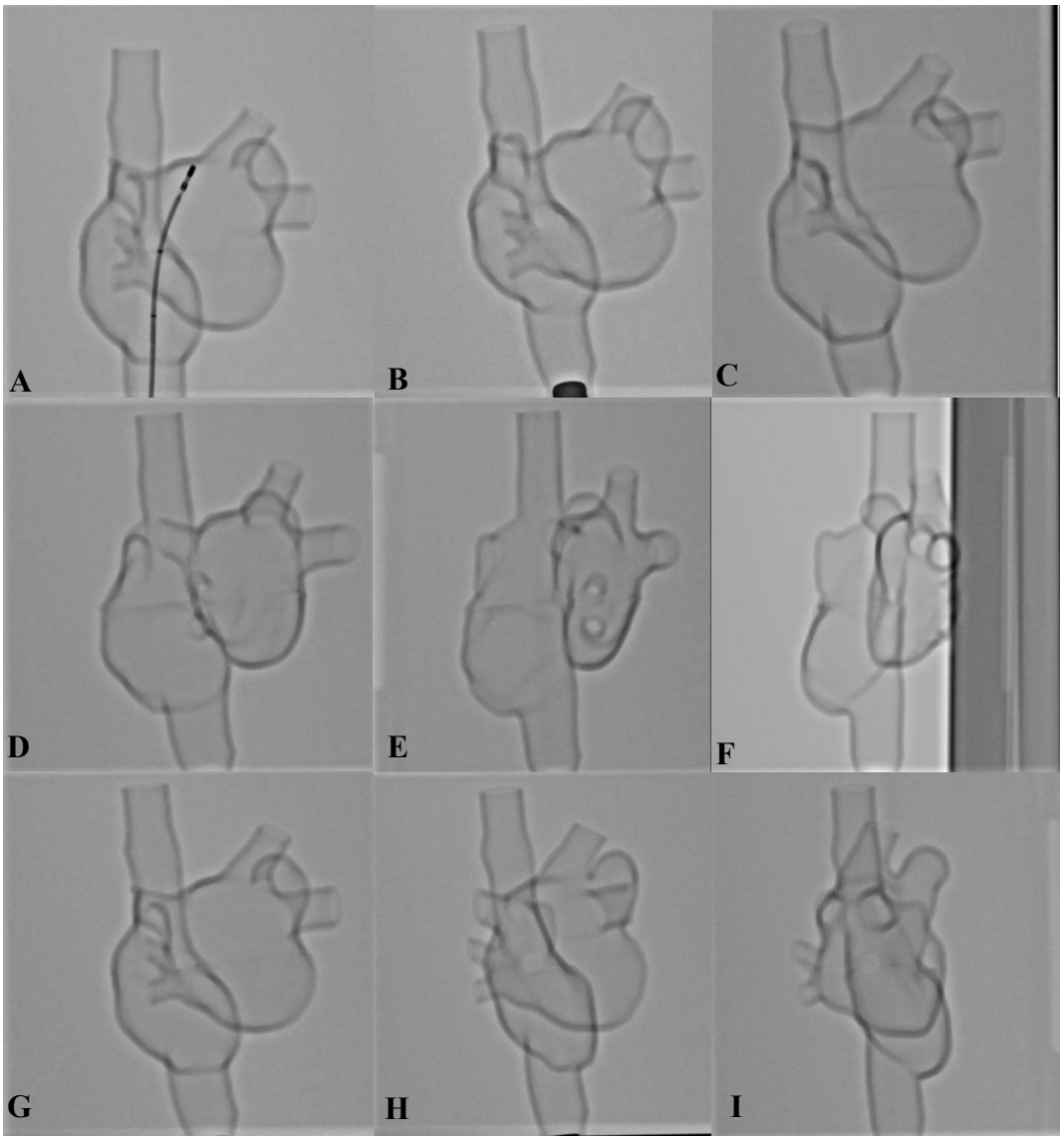


\

***Figure 38*** *Low-energy fluoroscopy images of the phantom captured using a clinical C-arm system:* ***A:*** *AP position with catheter.* ***B:*** *Cranial position.* ***C:*** *Caudal position.* ***D:*** *LAO 30°.* ***E:*** *LAO 60°.* ***F:*** *Left lateral 90°.* ***G:*** *RAO 30°. H: RAO 60°.* ***I:*** *Right lateral 90°.*

**Imaging the phantom using backlight**

In the backlight configuration, a light panel was placed behind the phantom and diffused using a sheet of paper. The AP, cranial, and caudal views yielded the highest quality images, with well-defined anatomical silhouettes and catheter positioning (**Figure 39 Parts A-C**.) LAO 30° produced a usable image, though minor quality degradation was noted. As the angle increased to LAO 60° and LAO 90°, image clarity deteriorated due to light leakage around the edges of the diffusion material, which overexposed parts of the image and reduced contrast (**Figure 39 Parts D-F)**. A similar pattern was observed in the RAO positions: RAO 30° remained moderately usable, but RAO 60° and RAO 90° suffered from image saturation and framing issues due to the fixed ROI, which did not maintain the phantom at the centre when the camera position changed. (**Figure 39 Parts G-I)**

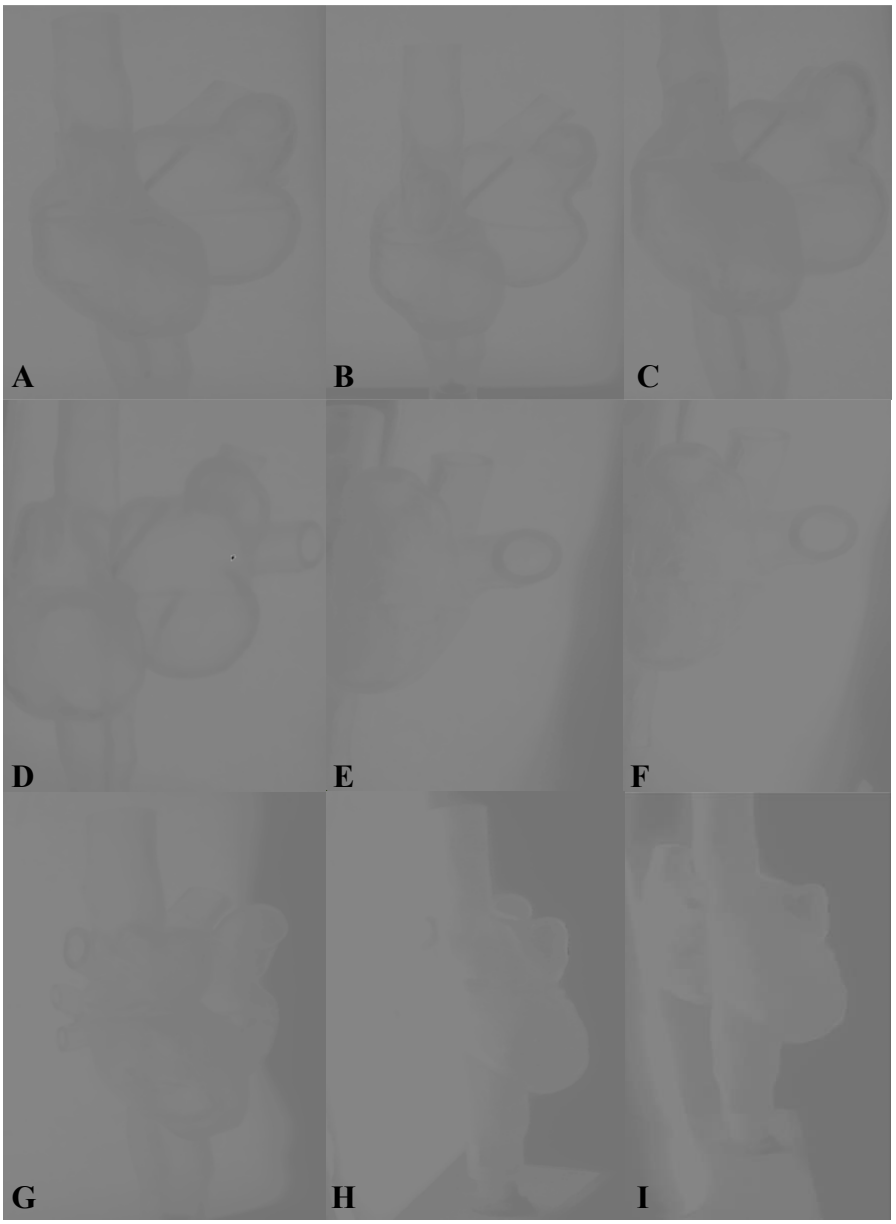


***Figure 39*** *C-Arm simulator images of the phantom captured using the backlight setup:* ***A:*** *AP position with catheter.* ***B:*** *Cranial position.* ***C:*** *Caudal position.* ***D:*** *LAO 30°.* ***E:*** *LAO 60°.* ***F:*** *Left lateral 90°.* ***G:*** *RAO 30°.* ***H:*** *RAO 60°.* ***I:*** *Right lateral 90°.*

**Imaging the phantom using a dynamic floodlight**

In the floodlight setup, a 150-lumen directional light source was mounted opposite the camera and manually repositioned to remain aligned with the imaging axis during rotation. This approach simulated the real C-arm configuration, in which the detector moves while the radiation source remains fixed. Usable images were obtained at AP, cranial, caudal, and LAO 30° positions (**Figure 40 Parts A-C)**. However, LAO 60° and LAO 90° were significantly overexposed and not usable due to the lack of consistent diffusion in the lighting path (**Figure 40 Parts D-F)**. RAO 30°, RAO 60°, and right lateral views were not attempted in this configuration, as preliminary tests showed severe light bleeding and image washout, which rendered them entirely unusable.

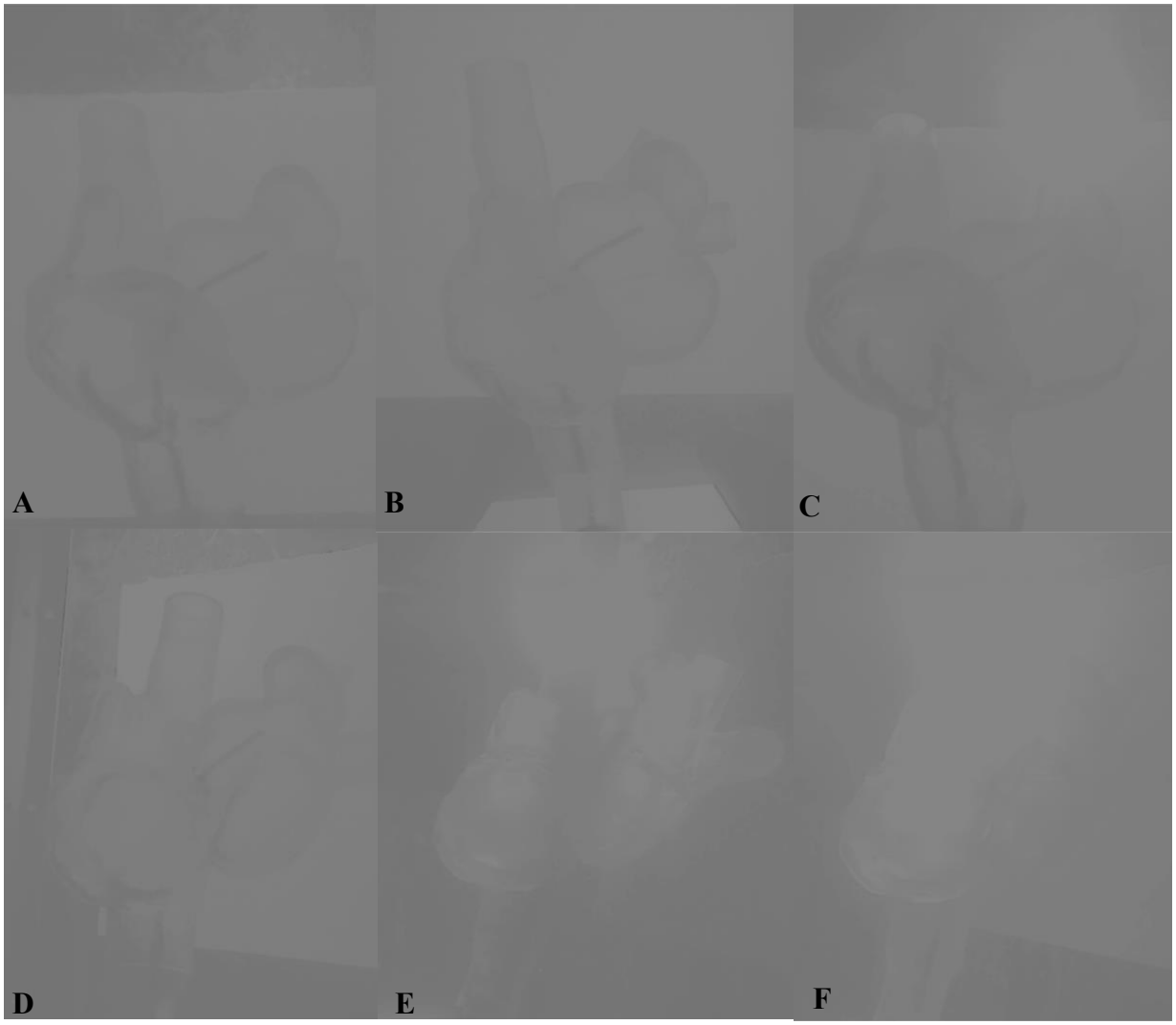


***Figure 40*** *C-Arm simulator images of the phantom captured using the dynamic moving floodlight setup:* ***A:*** *AP position with catheter.* ***B:*** *Cranial position.* ***C:*** *Caudal position.* ***D:*** *LAO 30°.* ***E:*** *LAO 60°.* ***F:*** *Left lateral 90°.*

**Overall performance and questionnaire**

The image processing pipeline remained stable and responsive throughout all trials. The wireless camera transmitted a real-time feed with minimal latency, and the ROI selection and system controls performed reliably. No delays, connection issues, or code errors were observed during testing. The simulator was operated in a dark room to enhance contrast and minimise environmental interference.

| Question | Metric Type | Participant 1 | Participant 2 |
|---|---|---|---|
| Image quality | 1-5 rating | 4 | 4 |
| Image issues | Qualitative | Poor contrast | None |
| Camera alignment | 1-5 rating | 4 | 4 |

***Table 3*** *Results from the Image Processing section of the questionnaire.*

Participant feedback was collected via a structured questionnaire. Both users, who had prior experience with real C-arm systems, rated the image quality an average of 4.5 out of 5. One participant noted occasional loss of contrast in certain views, while the other reported no visual issues. Camera alignment was also rated 4.5 out of 5 on average (**Table 3**). These subjective evaluations indicate a generally positive perception of the imaging system's realism and functionality, despite known limitations in certain imaging angles.

## 3.4 Usability, Portability, and General Feedback

The assembled simulator, including its rotating and support modules, was mounted on a 1250 mm × 650 mm plywood base and placed on a wheeled trolley to enable relocation. While no mechanical issues or structural failures occurred during transport, the system's centre of mass was situated near the top, which made movement physically challenging. Portability was assessed via a questionnaire completed by two participants. One participant rated portability as 3 out of 5, while the other rated it 2 out of 5, giving an average score of 2.5. Compactness was unanimously rated as 2 out of 5, with the physical footprint of the simulator identified as a limiting factor.

In terms of ease of use, participants gave an average score of 3.5 out of 5 for general system operation. The intuitiveness of the control system (the joystick and button interface) was rated 4 out of 5 by both participants. Both users indicated that they would consider the simulator suitable for training and testing applications (**Table 4**)

| **Question** | **Metric Type** | **Participant 1** | **Participant 2** |
|---|---|---|---|
| Portability | 1-5 rating | 3 | 2 |
| Compactness | 1-5 rating | 2 | 2 |
| Ease of operation | 1-5 rating | 4 | 3 |
| Intuitive control | 1-5 rating | 4 | 4 |
| Usability for Training / Testing | Yes/No | Yes | Yes |

***Table 4*** *Results from the Overall Usability section of the questionnaire.*

# 4. Discussion

## 4.1 Structural Stability and Mechanical Design Considerations

The mechanical construction of the C-arm simulator demonstrated functional robustness and mechanical reliability. All components performed as intended during testing, with no structural faults or mechanical failures observed. Both cranial–caudal and left–right angulations were executed smoothly, and motor-driven motion remained consistent and responsive. This was further supported by questionnaire results, where participants rated mechanical stability at 3.5 out of 5 and smoothness of movement in both directions at 4 out of 5, with no reports of resistance, instability, or mechanical glitches.

However, the simulator's design presented limitations. The central aluminium extrusion supporting the rotating and support modules, along with the C-arm, created a top-heavy structure, with the centre of mass located in front of the extrusion. Although securely fixed using eight self-tapping screws into a 1250 mm × 650 mm wooden base, this configuration may be insufficient under prolonged use or heavy loading, potentially posing a safety risk in case of mechanical failure. To enhance structural rigidity and safety, additional angled aluminium extrusions are recommended to redistribute weight and improve resistance to forward tilting. Such modifications would better prepare the system for transport and routine clinical training use.

The belt tensioning mechanism also presents an area for improvement. The current 3D-printed tensioner bracket, supported by a secondary printed piece, may degrade over time. Redesigning the tensioner with a fixed guiding channel terminating in a notch or divot would improve long-term stability. This refinement could be easily implemented through minor modifications to the CAD model and re-fabrication via laser cutting.

## 4.2 Reliability of the Electrical Control System

The electrical system performed reliably across all trials, with no failures, communication errors, or unintended behaviour observed. Motor control was smooth and immediate, and all programmed control features, including single, double, and triple button presses, operated as intended. The joystick provided precise manual control, with software-based dead zones effectively mitigating unintended inputs from minor hand tremors.

Electrical reliability was further enhanced by soldering all wire connections directly onto a custom Arduino-compatible shield, improving physical connection integrity compared to the initial breadboard prototype. This change also contributed to cleaner wiring layouts and improved long-term durability.

Participant feedback aligned with these observations, with both users reporting no issues regarding electrical performance. Wiring layout and accessibility were each rated 4 out of 5, reinforcing the conclusion that the electrical design was robust, user-friendly, and appropriate for prolonged operation.

## 4.3 Imaging Performance and Experimental Limitations

The simulated outputs were qualitatively compared against real fluoroscopic images captured from the same phantom at standard anatomical angles, serving as a reference for benchmarking.

Under the backlight configuration, imaging performance was satisfactory at anterior–posterior (AP), cranial, and caudal positions. Clear silhouettes and catheter visualisation were achieved. RAO 30° and LAO 30° images remained usable, although with reduced clarity. However, beyond LAO 60°, LAO 90°, RAO 60°, and RAO 90°, image quality deteriorated significantly. Primary sources of error identified in imaging performance included inconsistent backlight

positioning, phantom surface reflections, and ROI misalignment. The backlight remained stationary while the C-arm rotated, leading to reflections and overexposure. Additionally, a fixed ROI led to off-centred or partially cropped images as the camera moved. In the dynamic floodlight setup, only six angles were imaged (AP, cranial, caudal, LAO 30°, 60°, and 90°). Although AP, cranial, and caudal views were moderately usable, LAO 60° and 90° suffered from direct floodlight exposure causing severe image washout.

Despite these challenges, the image processing pipeline itself functioned reliably, with real-time performance and stable filtering effects. Participant evaluation rated image quality 4.5 out of 5 on average. However, it should be acknowledged that subjective ratings may have been influenced by the more successful imaging angles, and the limited sample size (n=2) restricts the generalisability of results. Environmental factors also affected output quality. The phantom's semi-transparent material properties limited internal feature visibility, and the use of a standard webcam with effective resolution loss due to ROI cropping further constrained image quality.

Future work should aim to address these limitations through dynamic lighting control, optical phantom improvements, and higher-quality imaging sensors. Additionally, quantitative benchmarking using structural similarity indices (SSIM) or feature-matching algorithms should be introduced to more rigorously assess simulator output.

Although CNN-based AI image enhancement was considered initially, it was not pursued due to computational constraints and scope limitations. Conventional image processing techniques combined with hardware improvements were sufficient to achieve the required visual realism for initial system validation.

## 4.4 Usability, Portability, and Design Considerations

The simulator received relatively low ratings for portability and compactness, scoring 2.5 and 2.0 out of 5, respectively. The oversized wooden base (1250 mm × 650 mm) hindered manoeuvrability and limited ease of transport through doorways or between rooms. Nonetheless, the hardware footprint was substantially reduced compared to previous versions, with the rotating module's volume decreased by 62.8%. The modular design—comprising a detachable rotating module, support component, C-arm, and base—enabled easier disassembly and reassembly.

In terms of usability, the joystick and button-based control system was rated highly. However, the absence of explicit labelling on the control interfaces was noted as a limitation. Although the spatial arrangement of buttons was logical, explicit labelling would further improve intuitiveness and accessibility. Another ergonomic issue arose from the use of a low-profile trolley, requiring users to crouch during operation. A smaller base would allow mounting on a taller trolley, improving both ergonomics and ease of use.

Overall, while the system functioned effectively, improvements in control labelling, base size, and mounting height are recommended for future iterations to enhance practicality and user experience.

## 4.5 Broader Implications, Ethics, and Sustainability

This project presents a low-cost, modular alternative to radiation-based imaging simulators, with significant socio-economic benefits in medical training and research contexts. Through the use of consumer-grade electronics, 3D-printed and laser-cut components, and a visible-light imaging approach, the system offers an affordable and accessible option for institutions lacking resources for conventional fluoroscopy equipment. Component-level cost considerations are detailed in Appendix D, reinforcing the simulator's low-cost design compared to cost of traditional C-Arm systems . These considerations directly informed the design of the simulator's modular architecture, sustainable fabrication processes, and radiation-free operation. From a sustainability perspective, the use of PLA filament and acrylic sheets supports low-waste manufacturing; however, the environmental impact could be further reduced by transitioning to recyclable PLA materials. The modular design also allows for easy replacement of parts, extending the system's operational lifespan and reducing e-waste.

The system was developed solely for benchtop educational use, without live subjects or ionising radiation. Consequently, no ethical approval was required. Nonetheless, further validation through larger cohort testing and structured safety assessments will be necessary before integration into regulated medical education programmes.

Future work should also explore more formalised image benchmarking protocols and incorporating quantitative methods such as SSIM analysis to validate image realism objectively.

# 5. Conclusions

This project successfully developed a modular, radiation-free C-arm simulator capable of generating X-ray-like images of transparent phantoms using visible light and real-time image processing. The simulator was constructed using 3D-printed and laser-cut components, integrated with a wireless webcam and a motorised positioning system, achieving substantial reductions in cost, complexity, and environmental impact compared to conventional fluoroscopy equipment.

The system demonstrated reliable mechanical and electrical performance, intuitive user control, and the ability to produce recognisable fluoroscopy-style images under controlled conditions. Structured user feedback further validated the system's stability and usability. However, critical limitations were identified in lighting control, phantom material transparency, imaging consistency at oblique angles, and the effective resolution loss due to fixed region-of-interest cropping. Additionally, the small sample size of user evaluations restricted the generalisability of findings.

Future work should focus on refining the imaging setup, introducing dynamic lighting calibration, improving phantom materials, and expanding user testing cohorts. Quantitative validation methods, such as structural similarity index (SSIM) analysis, are recommended to benchmark image realism rigorously. Overall, the simulator provides a strong foundation for further development into a sustainable, accessible training tool for medical imaging and interventional procedure education.

# 6. Future Works

## 6.1 Limitations

Several limitations were identified during the development and testing of the simulator. Lighting control across different viewing angles remained inconsistent, resulting in variable image quality, particularly at oblique positions. The semi-transparent phantom materials limited the visualisation of internal structures, constraining the simulator's ability to replicate true fluoroscopic imaging. The fixed region-of-interest (ROI) cropping led to effective resolution loss during off-axis imaging. Additionally, only two participants evaluated the system's usability, limiting the statistical significance of user feedback. Quantitative validation metrics were not implemented, relying instead on qualitative image comparisons. These limitations highlight areas requiring further refinement to enhance system realism, robustness, and educational value.

## 6.2 Future Scope

Future developments of the simulator should prioritise refining the imaging environment. A dynamic, repositionable lighting system is recommended to maintain consistent backlighting across all rotational angles. Optical improvements could be achieved through the use of higher-clarity phantom materials and enhanced camera sensors equipped with optical zoom functionality. Implementing dynamic ROI tracking would mitigate off-centre imaging issues and preserve image resolution during motion. Larger user testing cohorts, incorporating structured usability protocols, should be conducted to validate system performance more rigorously. Quantitative benchmarking using methods such as structural similarity index (SSIM) analysis or feature-based matching algorithms would enable objective evaluation of image realism. Furthermore, integrating AI-based post-processing could be explored in future

versions once baseline imaging consistency is achieved. These enhancements would support the evolution of the simulator into a reliable, sustainable tool for surgical training and procedural planning.

# 7. Bibliography


[1] M. Berger, Q. Yang, and A. Maier, "X-ray Imaging," in Medical Imaging Systems, vol. 11111, A. Maier, S. Steidl, V. Christlein, and J. Hornegger, Eds., in Lecture Notes in Computer Science, vol. 11111. , Cham: Springer International Publishing, 2018, pp. 119–145. doi: 10.1007/978-3-319-96520-8_7.

[2] C. J. Harvey, "Principles of radiology," *Surgery (Oxford)*, vol. 26, no. 6, pp. 235–238, Jun. 2008, doi: 10.1016/j.mpsur.2008.04.008.

[3] B. Buchberger, K. Scholl, L. Krabbe, L. Spiller, and B. Lux, "Radiation exposure by medical X-ray applications," *GMS German Medical Science*, vol. 20, 2022, doi: 10.3205/000308.

[4] J. D. Hout and J. Ryu, "The association between musculoskeletal disorders and lead apron use in healthcare workers: A systematic review and meta-analysis," *Safety Science*, vol. 181, p. 106669, Jan. 2025, doi: 10.1016/j.ssci.2024.106669.

[5] M. Zuguchi, K. Chida, M. Taura, Y. Inaba, A. Ebata, and S. Yamada, "Usefulness of non-lead aprons in radiation protection for physicians performing interventional procedures," *Radiation Protection Dosimetry*, vol. 131, no. 4, pp. 531–534, Jul. 2008, doi: 10.1093/rpd/ncn244.

[6] D. G. Rizik *et al.*, "Comprehensive Radiation Shield Minimizes Operator Radiation Exposure and Obviates Need for Lead Aprons," *Journal of the Society for Cardiovascular Angiography & Interventions*, vol. 2, no. 3, p. 100603, May 2023, doi: 10.1016/j.jscai.2023.100603.

[7] J. Yang *et al.*, "Development and experimental verification of C-arm camera shooting locator," *Sci Rep*, vol. 12, no. 1, p. 22222, Dec. 2022, doi: 10.1038/s41598-022-26286-9.

[8] C. M. Stahl, Q. C. Meisinger, M. P. Andre, T. B. Kinney, and I. G. Newton, "Radiation Risk to the Fluoroscopy Operator and Staff," *American Journal of Roentgenology*, vol. 207, no. 4, pp. 737–744, Oct. 2016, doi: 10.2214/AJR.16.16555.

[9] M. I. Balonov and P. C. Shrimpton, "Effective dose and risks from medical x-ray procedures," *Annals of the ICRP*, vol. 41, no. 3–4, pp. 129–141, Oct. 2012, doi: https://doi.org/10.1016/j.icrp.2012.06.002.

[10] P. Rajaraman *et al.*, "Cancer Risks in U.S. Radiologic Technologists Working With Fluoroscopically Guided Interventional Procedures, 1994-2008," *AJR. American journal of roentgenology*, vol. 206, no. 5, pp. 1101–1108; quiz 1109, May 2016, doi: https://doi.org/10.2214/AJR.15.15265.

[11] S. Andrew, M. R. Abdelmonem, S. Kohli, and H. Dabke, "Evaluation of Back Pain and Lead Apron Use Among Staff at a District General Hospital," *Cureus*, Oct. 2021, doi: https://doi.org/10.7759/cureus.18859.

[12] Maghrabi, Huda & Deb, Pradip & Vijayan, Arun & Wang, Lijing. (2015). Maghrabi, H.,Deb, P.,Vijayan, A.,Wang, L. (2015). An overview of lead aprons for radiation protection: are they doing their best? In: Proceedings of the 8th Textile Bioengineering and Informatics Symposium (TBIS 2015), Zadar, Croatia, 14-17 June 2015.

[13] R. S. Livingstone, A. Varghese, and S. N. Keshava, "A Study on the Use of Radiation-Protective Apron among Interventionists in Radiology," *Journal of Clinical Imaging Science*, vol. 8, p. 34, Aug. 2018, doi: 10.4103/jcis.JCIS_34_18.

[14] R. J. Hurley, F. J. McCabe, L. Turley, D. Maguire, J. Lucey, and C. J. Hurson, "Whole-body radiation exposure in Trauma and Orthopaedic surgery," *Bone & Joint Open*, vol. 3, no. 11, pp. 907–912, Nov. 2022, doi: 10.1302/2633-1462.311.BJO-2022-0062.R1.

[15] R. G. Dixon *et al.*, "Society of Interventional Radiology: Occupational Back and Neck Pain and the Interventional Radiologist," *Journal of Vascular and Interventional Radiology*, vol. 28, no. 2, pp. 195–199, Feb. 2017, doi: https://doi.org/10.1016/j.jvir.2016.10.017.

[16] B. Siewert, O. R. Brook, M. M. Mullins, R. L. Eisenberg, and J. B. Kruskal, "Practice Policy and Quality Initiatives: Strategies for Optimizing Staff Safety in a Radiology Department," *RadioGraphics*, vol. 33, no. 1, pp. 245–261, Jan. 2013, doi: 10.1148/rg.331125174.

[17] W. J. Davros, "Fluoroscopy: basic science, optimal use, and patient/operator protection," *Techniques in Regional Anesthesia and Pain Management*, vol. 11, no. 2, pp. 44–54, Apr. 2007, doi: 10.1053/j.trap.2007.02.005.

[18] J. Hughes, *C-arm systems*, vol. 1. Oxford University Press, 2018. doi: 10.1093/med/9780198813170.003.0002.

[19] I. Lemammer, O. Michel, H. Ayasso, S. Zozor, and G. Bernard, "Online mobile C-arm calibration using inertial sensors: a preliminary study in order to achieve CBCT," *Int J CARS*, vol. 15, no. 2, pp. 213–224, Feb. 2020, doi: 10.1007/s11548-019-02061-6.

[20] N. E. Shalom, G. X. Gong, and M. Auster, "Fluoroscopy: An essential diagnostic modality in the age of high-resolution cross-sectional imaging," *WJR*, vol. 12, no. 10, pp. 213–230, Oct. 2020, doi: 10.4329/wjr.v12.i10.213.

[21] K. Cleary, A. Melzer, V. Watson, G. Kronreif, and D. Stoianovici, "Interventional robotic systems: Applications and technology state-of-the-art," *Minimally Invasive Therapy & Allied Technologies*, vol. 15, no. 2, pp. 101–113, Jan. 2006, doi: 10.1080/13645700600674179.

[22] Allen, Daniel R., "Simulation Approaches to X-ray C-Arm-based Interventions" (2020). Electronic Thesis and Dissertation Repository. 7231.

[23] W. Birkfellner *et al.*, “Fast DRR Generation for 2D/3D Registration,” in *Medical Image Computing and Computer-Assisted Intervention – MICCAI 2005*, vol. 3750, J. S. Duncan and G. Gerig, Eds., in Lecture Notes in Computer Science, vol. 3750. , Berlin, Heidelberg: Springer Berlin Heidelberg, 2005, pp. 960–967. doi: 10.1007/11566489_118.

[24] M. Unberath *et al.*, “Enabling machine learning in X-ray-based procedures via realistic simulation of image formation,” *Int J CARS*, vol. 14, no. 9, pp. 1517–1528, Sep. 2019, doi: 10.1007/s11548-019-02011-2.

[25] O. J. Bott *et al.*, “virtX – Evaluation of a Computer-based Training System for Mobile C-arm Systems in Trauma and Orthopedic Surgery,” *Methods Inf Med*, vol. 47, no. 03, pp. 270–278, 2008, doi: 10.3414/ME0476.

[26] R. H. Gong, B. Jenkins, R. W. Sze, and Z. Yaniv, “A cost effective and high fidelity fluoroscopy simulator using the Image-Guided Surgery Toolkit (IGSTK),” presented at the SPIE Medical Imaging, Z. R. Yaniv and D. R. Holmes, Eds., San Diego, California, USA, Mar. 2014, p. 903618. doi: 10.1117/12.2044112.

[27] A. R. Faulkner, A. C. Bourgeois, Y. C. Bradley, and A. S. Pasciak, “A Robust and Inexpensive Phantom for Fluoroscopically Guided Lumbar Puncture Training,” *Simulation in Healthcare: The Journal of the Society for Simulation in Healthcare*, vol. 10, no. 1, pp. 54–58, Feb. 2015, doi: 10.1097/SIH.0000000000000066.

[28] N. M. W. Dwara, M. R. Mak’ruf, and T. B. Indrato, “Utilization of Webcam Cameras as X-Ray Image Capture (kV Settings and Shutter Sensors),” *Indones.J.electronic.electromed.med.inf*, vol. 5, no. 3, pp. 144–150, Aug. 2023, doi: 10.35882/ijeeemi.v5i3.290.

[29] C. A. Vega Mernes, I. G. Francelino, E. M. Kakuno, and M. G. Hönnicke, “A simple and low cost USB webcam-driven optical tomography system suitable for teaching x-ray computed tomography,” *Eur. J. Phys.*, vol. 42, no. 4, p. 045301, Jul. 2021, doi: 10.1088/1361-6404/abf021.

[30] M. Haiderbhai *et al.*, “pix2xray: converting RGB images into X-rays using generative adversarial networks,” *Int J CARS*, vol. 15, no. 6, pp. 973–980, Jun. 2020, doi: 10.1007/s11548-020-02159-2.

[31] Ideen Sadrehaghighi ANNAPOLIS, “Computer Aided Design (CAD),” 2022, doi: 10.13140/RG.2.2.12634.62408.

[32] J. M. Fiore, “Laboratory Manual for Embedded Controllers Using C and Arduino”.

[33] Hussain, Dr. S.. (2015). Automated Color Recognition System for Visually Challenged and Achromatopsia People using Arduino and Mobile App. 4. 2278-909.

[34] B. Aranjo, P. K. Soori, and P. Talukder, “Stepper motor drives for robotic applications,” in *2012 IEEE International Power Engineering and Optimization Conference*, Melaka, Malaysia: IEEE, Jun. 2012, pp. 361–366. doi: 10.1109/PEOCO.2012.6230890.

[35] T. Muangpool and S. Pullteap, “Reviews on laser cutting technology for industrial applications,” in *Third International Conference on Photonics Solutions (ICPS2017)*, T. Mayteevarunyoo, Ed., Pattaya, Thailand: SPIE, Mar. 2018, p. 34. doi: 10.1117/12.2300955.

[36] N. Shahrubudin, T. C. Lee, and R. Ramlan, “An Overview on 3D Printing Technology: Technological, Materials, and Applications,” *Procedia Manufacturing*, vol. 35, pp. 1286–1296, 2019, doi: 10.1016/j.promfg.2019.06.089.

# 8.Appendices

## Appendix A: 8.1 Questionnaire Results

## Participant 1

### C-ARM Simulator Evaluation Questionnaire

*Your responses will remain anonymous and will only be used for research and development purposes.*

**Section 1: Participant Information**

1. **What is your background?** *(Select one or more)*

☐Medical Student

☐Radiologist

☒Biomedical Engineer

☐Clinician

☐Other

2. **Have you used real C-ARM systems before?**

☒Yes, regularly

☐Yes, but infrequently

☐No

**Section 2: Mechanical Performance & Robustness**

3. **How would you rate the mechanical stability of the simulator?**

*(1 = Unstable, 5 = Very stable)*

☐1

☐2

☐3

☒4

☐5

4. **How smooth is the movement of the C-ARM in the following axes?** *(Rate each separately)*

| Movement Type | Very Jerky (1) | (2) | (3) | (4) | Very Smooth (5) |
|---|---|---|---|---|---|
| **Vertical (height) movement** | ☐ | ☐ | ☐ | ☒ | ☐ |
| **Rotational (angular) movement** | ☐ | ☐ | ☐ | ☒ | ☐ |

5. **Did you experience any mechanical resistance, backlash, or instability?** *(Check all that apply)*

☐Yes, resistance in vertical movement

☐Yes, resistance in rotational movement

☐Yes, instability in structure

☒No issues observed

**Section 3: Electronics & Control System**

6. **How responsive was the control system?** *(1 = Poor responsiveness, 5 = Immediate and accurate response)*

☐1

☐2

☐3

☐4

☒5

7. **Did you observe any of the following electronic issues?** *(Check all that apply)*

☐Delays in motor response

☐Unexpected shutdowns

☒No issues

8. **How well organised and accessible were the electronic components and wiring?** *(1 = Very disorganised, 5 = Well-structured and accessible)*

☐1

☐2

☐3

☒4

☐5

**Section 4: Imaging System & Camera Performance**

9. **How would you rate the quality of the images produced?** *(1 = Poor, 5 = Excellent)*

☐1

☐2

☐3

☒4

☐5

10. **Did you notice any of the following imaging issues?** *(Check all that apply)*

☐Blurry images

☐Poor contrast

☐Distortions or artifacts

☐Inconsistent lighting conditions

☒No issues

11. **How would you rate the positioning and alignment of the camera for imaging?** *(1 = Misaligned, 5 = Perfectly aligned)*

☐1

☐2

☐3

☒4

☐5

**Section 5: Portability & Ease of Use**

12. **How portable is the C-ARM simulator in its current design?** *(1 = Not portable, 5 = Very easy to transport and set up)*

☐1

☐2

☒3

☐4

☐5

13. **How compact is the system for storage and mobility?** *(1 = Bulky and difficult to store, 5 = Compact and easy to store)*

☐1

☒2

☐3

☐4

☐5

**Section 6: Usability & Overall Experience**

14. **How easy was it to operate the simulator?** *(1 = Very difficult, 5 = Very easy)*

☐1

☐2

☐3

☒4

☐5

15. **How intuitive was the user interface and control system?** *(1 = Not intuitive at all, 5 = Very intuitive)*

☐1

☐2

☐3

☒4

☐5

16. **Would you consider this simulator useful for training and testing purposes?**

☒Yes

☐No

# Participant 2

## C-ARM Simulator Evaluation Questionnaire

*Your responses will remain anonymous and will only be used for research and development purposes.*

**Section 1: Participant Information**

1. **What is your background?** *(Select one or more)*

☐Medical Student

☐Radiologist

☒Biomedical Engineer

☐Clinician

☐Other

2. **Have you used real C-ARM systems before?**

☐Yes, regularly

☒Yes, but infrequently

☐No

**Section 2: Mechanical Performance & Robustness**

3. **How would you rate the mechanical stability of the simulator?**

*(1 = Unstable, 5 = Very stable)*

☐1

☐2

☒3

☐4

☐5

4. **How smooth is the movement of the C-ARM in the following axes?** *(Rate each separately)*

| Movement Type | Very Jerky (1) | (2) | (3) | (4) | Very Smooth (5) |
|---|---|---|---|---|---|
| **Vertical (height) movement** | ☐ | ☐ | ☐ | ☒ | ☐ |
| **Rotational (angular) movement** | ☐ | ☐ | ☐ | ☒ | ☐ |

5. **Did you experience any mechanical resistance, backlash, or instability?** *(Check all that apply)*

☐Yes, resistance in vertical movement

☐Yes, resistance in rotational movement

☐Yes, instability in structure

☒No issues observed

**Section 3: Electronics & Control System**

6. **How responsive was the control system?** *(1 = Poor responsiveness, 5 = Immediate and accurate response)*

☐1

☐2

☐3

☐4

☒5

7. **Did you observe any of the following electronic issues?** *(Check all that apply)*

☐Delays in motor response

☐Inconsistent control inputs

☐Unstable power supply

☐Unexpected shutdowns

☒No issues

8. **How well organised and accessible were the electronic components and wiring?** *(1 = Very disorganised, 5 = Well-structured and accessible)*

☐1

☐2

☐3

☒4

☐5

**Section 4: Imaging System & Camera Performance**

9. **How would you rate the quality of the images produced?** *(1 = Poor, 5 = Excellent)*

☐1

☐2

☐3

☒4

☐5

10. **Did you notice any of the following imaging issues?** *(Check all that apply)*

☐Blurry images

☒Poor contrast

☐Distortions or artifacts

☐Inconsistent lighting conditions

☐No issues

11. **How would you rate the positioning and alignment of the camera for imaging?** *(1 = Misaligned, 5 = Perfectly aligned)*

☐1

☐2

☐3

☒4

☐5

**Section 5: Portability & Ease of Use**

12. **How portable is the C-ARM simulator in its current design?** *(1 = Not portable, 5 = Very easy to transport and set up)*

☐ 1

☒ 2

☐ 3

☐ 4

☐ 5

13. **How compact is the system for storage and mobility?** *(1 = Bulky and difficult to store, 5 = Compact and easy to store)*

☐ 1

☒ 2

☐ 3

☐ 4

☐ 5

**Section 6: Usability & Overall Experience**

14. **How easy was it to operate the simulator?** *(1 = Very difficult, 5 = Very easy)*

☐ 1

☐ 2

☒ 3

☐ 4

☐ 5

15. **How intuitive was the user interface and control system?** *(1 = Not intuitive at all, 5 = Very intuitive)*

☐ 1

☐ 2

☐ 3

☒ 4

☐ 5

16. **Would you consider this simulator useful for training and testing purposes?**



☒ Yes

☐ No

# Appendix B: 8.2 Motor Control Code

```
#include <AccelStepper.h>
#include <EEPROM.h>

// Pin definitions
const int stepPinX = 4;
const int dirPinX  = 3;
const int enPinX   = 2;

const int stepPinY = 5;
const int dirPinY  = 6;
const int enPinY   = 7;

const int joyXPin = A3;
const int joyYPin = A2;

const int button1 = 10; // LAO positions
const int button2 = 11; // RAO positions
const int button3 = 12; // Cranial/Caudal
const int button4 = 9;  // AP / 90° Right/Left
// Constants
const int joyCenter    = 512;
const int joyDeadZone  = 100;
const int maxSteps_X   = 5882;  // ±120°
const int maxSteps_Y   = 6400;  // ±2 revolutions for Y-axis
const float maxAngle_X = 120.0;
const float maxAngle_Y = 60.0;
const int doublePressTime = 500;  // Increased to 500ms between presses

// Set manual joystick speeds to match preset speed (400)
const int manualMaxSpeedX = 400;
const int manualMaxSpeedY = 400;

// Stepper motor instances (using DRIVER mode)
AccelStepper stepperX(AccelStepper::DRIVER, stepPinX, dirPinX);
AccelStepper stepperY(AccelStepper::DRIVER, stepPinY, dirPinY);

// Preset positions structure and array
struct PresetPosition {
```

```
  const char *name;
  long x_steps;
  long y_steps;
};
PresetPosition presets[] = {
  {"AP View (0°)", 0, 0},
  {"LAO 30°", -maxSteps_X * 0.25, 0},
  {"LAO 60°", -maxSteps_X * 0.5, 0},
  {"RAO 30°", maxSteps_X * 0.25, 0},
  {"RAO 60°", maxSteps_X * 0.5, 0},
  {"Cranial", 0, maxSteps_Y * 0.5},
  {"Caudal", 0, -maxSteps_Y * 0.5},
  {"90° Right", maxSteps_X * 0.65, 0},
  {"90° Left", -maxSteps_X * 0.65, 0}
};

// Button state structure for non-blocking detection
struct ButtonState {
  bool lastState;
  unsigned long lastPressTime;
  int pressCount;
};

ButtonState btn1 = {HIGH, 0, 0};
ButtonState btn2 = {HIGH, 0, 0};
ButtonState btn3 = {HIGH, 0, 0};
ButtonState btn4 = {HIGH, 0, 0};

// Mode flag: if presetActive is true, the steppers are executing a preset move.
// In manual mode (presetActive false) the joystick controls the motor speed.
bool presetActive = false;

// Timer for angle printing
unsigned long lastAnglePrintTime = 0;

// Function prototypes
void updateButtonState(ButtonState &state, int buttonPin, int shortPressIndex, int doublePressIndex, int
triplePressIndex = -1);
void moveToPreset(int index);
void displayAngles();
```

```
void processJoystick();

void setup() {
  // Enable motor drivers
  pinMode(enPinX, OUTPUT);
  digitalWrite(enPinX, LOW);
  pinMode(enPinY, OUTPUT);
  digitalWrite(enPinY, LOW);

  // Set button pins as INPUT_PULLUP
  pinMode(button1, INPUT_PULLUP);
  pinMode(button2, INPUT_PULLUP);
  pinMode(button3, INPUT_PULLUP);
  pinMode(button4, INPUT_PULLUP);

  // Set up steppers
  stepperX.setMaxSpeed(400);
  stepperX.setAcceleration(1000);
  stepperY.setMaxSpeed(400);
  stepperY.setAcceleration(1000);

  Serial.begin(9600);
  Serial.println("Setup complete. Restoring last position...");

  // Restore last position from EEPROM
  long lastX, lastY;
  EEPROM.get(0, lastX);
  EEPROM.get(sizeof(long), lastY);

  // Validate restored positions; if out of bounds, reset to 0.
  if (lastX < -maxSteps_X || lastX > maxSteps_X || lastY < -maxSteps_Y || lastY > maxSteps_Y) {
    lastX = 0;
    lastY = 0;
  }
  stepperX.setCurrentPosition(lastX);
  stepperY.setCurrentPosition(lastY);

  Serial.print("Restored Position -> X: ");
  Serial.print(lastX);
  Serial.print(" | Y: ");
```

```
  Serial.println(lastY);
  displayAngles();
}

void loop() {
  // Update button states to detect preset move commands.
  updateButtonState(btn1, button1, 1, 2);
  updateButtonState(btn2, button2, 3, 4);
  updateButtonState(btn3, button3, 5, 6);
  // For the AP button (button4): short press = AP view, double press = 90° Right, triple press = 90° Left.
  updateButtonState(btn4, button4, 0, 7, 8);

  // Read joystick input.
  int joyX = analogRead(joyXPin);
  int joyY = analogRead(joyYPin);

  // Determine if joystick is active (outside the deadzone for either axis).
  bool joystickActive = (abs(joyX - joyCenter) > joyDeadZone || abs(joyY - joyCenter) > joyDeadZone);

  if (joystickActive) {
    // Override any preset move.
    presetActive = false;
    processJoystick();
  } else {
    // If no joystick input and not in a preset move, stop the motors.
    if (!presetActive) {
      stepperX.setSpeed(0);
      stepperY.setSpeed(0);
    }
  }

  // If a preset move is active, use position control.
  if (presetActive) {
    stepperX.run();
    stepperY.run();
    if (abs(stepperX.distanceToGo()) < 5 && abs(stepperY.distanceToGo()) < 5) {
      presetActive = false;
      long newX = stepperX.currentPosition();
      long newY = stepperY.currentPosition();
      EEPROM.put(0, newX);
```

```
      EEPROM.put(sizeof(long), newY);
    }
  } else {
    // In manual (joystick) mode, run the motors based on set speeds.
    stepperX.runSpeed();
    stepperY.runSpeed();
  }

  // Always print the current angles every 100ms.
  if (millis() - lastAnglePrintTime > 100) {
    displayAngles();
    lastAnglePrintTime = millis();
  }
}

// processJoystick() maps the joystick values to motor speeds.
// If both axes are active (diagonal), only the dominant axis is used.
void processJoystick() {
  int joyX = analogRead(joyXPin);
  int joyY = analogRead(joyYPin);

  int diffX = joyX - joyCenter;
  int diffY = joyY - joyCenter;

  long speedX = 0;
  long speedY = 0;

  bool xActive = (abs(diffX) > joyDeadZone);
  bool yActive = (abs(diffY) > joyDeadZone);

  // Calculate speeds for each axis if active.
  if (xActive) {
    if (diffX > 0) {
      speedX = map(joyX, joyCenter + joyDeadZone, 1023, 0, manualMaxSpeedX);
    } else {
      speedX = map(joyX, 0, joyCenter - joyDeadZone, -manualMaxSpeedX, 0);
    }
  }

  if (yActive) {
```

```
    if (diffY > 0) {
      speedY = map(joyY, joyCenter + joyDeadZone, 1023, 0, manualMaxSpeedY);
    } else {
      speedY = map(joyY, 0, joyCenter - joyDeadZone, -manualMaxSpeedY, 0);
    }
  }

  // If both axes are active, only use the one with the larger deviation.
  if (xActive && yActive) {
    if (abs(diffX) > abs(diffY)) {
      speedY = 0;
    } else if (abs(diffY) > abs(diffX)) {
      speedX = 0;
    } else {
      // If they are equal, set both to zero.
      speedX = 0;
      speedY = 0;
    }
  }

  // Enforce positional limits.
  if (speedX > 0 && stepperX.currentPosition() >= maxSteps_X) {
    speedX = 0;
  }
  if (speedX < 0 && stepperX.currentPosition() <= -maxSteps_X) {
    speedX = 0;
  }
  if (speedY > 0 && stepperY.currentPosition() >= maxSteps_Y) {
    speedY = 0;
  }
  if (speedY < 0 && stepperY.currentPosition() <= -maxSteps_Y) {
    speedY = 0;
  }

  stepperX.setSpeed(speedX);
  stepperY.setSpeed(speedY);
}

// updateButtonState() detects short, double, or triple presses non-blocking.
// Once the press count is finalised, it calls moveToPreset() with the corresponding preset index.
```

```
void updateButtonState(ButtonState &state, int buttonPin, int shortPressIndex, int doublePressIndex, int
triplePressIndex) {
  bool currentState = digitalRead(buttonPin);
  unsigned long currentTime = millis();

  // Detect falling edge (button press, active LOW).
  if (state.lastState == HIGH && currentState == LOW) {
    if (currentTime - state.lastPressTime > doublePressTime) {
      state.pressCount = 1;
      state.lastPressTime = currentTime;
    } else {
      state.pressCount++;
      state.lastPressTime = currentTime;
    }
  }

  // When the button is released and no new press occurs within doublePressTime, process the count.
  if (currentState == HIGH && state.pressCount > 0 && (currentTime - state.lastPressTime > doublePressTime)) {
    if (state.pressCount == 1) {
      moveToPreset(shortPressIndex);
    } else if (state.pressCount == 2) {
      moveToPreset(doublePressIndex);
    } else if (state.pressCount == 3 && triplePressIndex != -1) {
      moveToPreset(triplePressIndex);
    }
    state.pressCount = 0;
  }

  state.lastState = currentState;
}

// moveToPreset() sets a positional move for the steppers based on the preset.
void moveToPreset(int index) {
  Serial.print("Moving to preset: ");
  Serial.println(presets[index].name);
  stepperX.moveTo(presets[index].x_steps);
  stepperY.moveTo(presets[index].y_steps);
  presetActive = true;
}
```

```
// displayAngles() calculates and prints the current C-arm angles.
void displayAngles() {
  float angleX = (float)stepperX.currentPosition() / maxSteps_X * maxAngle_X;
  float angleY = (float)stepperY.currentPosition() / maxSteps_Y * maxAngle_Y;
  Serial.print("C-Arm Angles -> X: ");
  Serial.print(angleX, 1);
  Serial.print("° | Y: ");
  Serial.print(angleY, 1);
  Serial.println("°");
}
```

# Appendix C: 8.3 Image Processing Code

```
import cv2
import numpy as np

# Global cropping variables
crop_x, crop_y, crop_w, crop_h = 0, 0, 0, 0
prev_edges = None  # Store the previous frame's edges for temporal smoothing

def select_crop_region(frame):
    """Allow user to select a region to crop before processing starts."""
    global crop_x, crop_y, crop_w, crop_h
    roi = cv2.selectROI("Select Crop Region", frame, fromCenter=False, showCrosshair=True)
    cv2.destroyWindow("Select Crop Region")  # Close the selection window

    if roi != (0, 0, 0, 0):  # Ensure a valid selection
        crop_x, crop_y, crop_w, crop_h = roi

def suppress_reflections(frame):
    """Applies filtering to reduce reflections before processing."""
    return cv2.GaussianBlur(frame, (5,5), 0)

def enhance_xray_effect(frame):
    """Flattens background & foreground while making the phantom edges black and steady."""
    global crop_x, crop_y, crop_w, crop_h, prev_edges

    # Crop the frame if a region was selected
    if crop_w > 0 and crop_h > 0:
        frame = frame[crop_y:crop_y + crop_h, crop_x:crop_x + crop_w]

    # Suppress reflections
    frame = suppress_reflections(frame)

    # Convert to grayscale
    gray = cv2.cvtColor(frame, cv2.COLOR_BGR2GRAY)

    # Normalize brightness to bring background & foreground to the same grey level
    normalized = cv2.normalize(gray, None, 100, 120, cv2.NORM_MINMAX)

    # Apply Sobel edge detection to highlight only the phantom edges
    sobelx = cv2.Sobel(normalized, cv2.CV_64F, 1, 0, ksize=3)
    sobely = cv2.Sobel(normalized, cv2.CV_64F, 0, 1, ksize=3)
    sobel_edges = cv2.magnitude(sobelx, sobely)
    sobel_edges = np.uint8(np.clip(sobel_edges, 0, 255))

    # Apply thresholding to extract **only** steady, thin phantom edges
    _, edge_mask = cv2.threshold(sobel_edges, 35, 255, cv2.THRESH_BINARY)

    # Invert edges to make them black instead of white
    edge_mask = cv2.bitwise_not(edge_mask)

    # Apply temporal smoothing to stabilize edges across frames
    if prev_edges is None:
        prev_edges = edge_mask.copy()
    else:
        edge_mask = cv2.addWeighted(prev_edges, 0.6, edge_mask, 0.4, 0)
        prev_edges = edge_mask.copy()

    # Blend edges onto the flattened grey image
    blended = cv2.addWeighted(normalized, 0.9, edge_mask, 0.1, 0)

    # Flip the final output horizontally for correct fluoroscopy orientation
    flipped = cv2.flip(blended, 1)

    return flipped

# Initialize webcam
cap = cv2.VideoCapture(0)  # Use 0 for default webcam, change if needed

if not cap.isOpened():
    print("Error: Could not access the webcam.")
    exit()

# Get an initial frame for cropping selection
ret, frame = cap.read()
if ret:
    select_crop_region(frame)  # Let user choose crop area
```

```
while True:
    ret, frame = cap.read()
    if not ret:
        print("Error: Failed to capture image.")
        break

    # Process the frame for a fluoroscopy effect
    processed_frame = enhance_xray_effect(frame)

    # Display the processed output
    cv2.imshow("Real-Time Fluoroscopy (Flipped, Black Edges, Grey Background)", processed_frame)

    key = cv2.waitKey(1) & 0xFF

    if key == ord('q'):  # Quit on 'q'
        break
    elif key == ord('r'):  # Reset cropping and allow re-selection
        select_crop_region(frame)

# Release the webcam and close all windows
cap.release()
cv2.destroyAllWindows()
```

# Appendix D: 8.4 Table of Components

| Part Name | Cost (£) | Project Fund |
|---|---|---|
| Stepper Motor (NEMA 23) | 23.99 | BEng Project |
| 10mm Bore Bearings | 8.99 | KURF |
| Electronics Enclosure | 9.99 | BEng Project |
| Cast Acrylic Sheet (Perspex) | 22.01 | KURF |
| TB6600 Stepper Driver | 14.99 | KURF |
| Joystick Module | 10.99 | BEng Project |
| Timing Belt Pulley (10mm Bore) | 9.59 | KURF |
| Power Supply 24V 15A | 29.99 | KURF |
| Timing Belt (Synchronous) | 7.99 | BEng Project |
| Solid Core Wires | 6.99 | BEng Project |
| Breadboard Power Module | 5.49 | BEng Project |
| Power Extension Cable | 8.99 | BEng Project |
| Tactile Push Buttons | 3.99 | BEng Project |
| Wireless Webcam (Toallin) | 126.99 | BEng Project |
| LED Floodlight | 15.99 | BEng Project |
| PLA Filament (1KG) | 17.99 | KURF |
| Stepper Motor (NEMA 17) | 13.49 | KURF |
| Aluminium Extrusions | 27.99 | KURF |
| Rubber Tubing | 5.99 | KURF |
| Overall Total | 376.43 | |
| Total under KURF budget | 151.03 | |
| Total under BEng budget | 225.40 | |

***Table 5*** *List of Components and their cost.*